Thermospheric and Ionospheric Effects by Gravity Waves from the Lower Atmosphere

H.-L. Liu[1], P. E. Lauritzen[2], F. Vitt[1,3] and S. Goldhaber[2]

[1]High Altitude Observatory, National Center for Atmospheric Research, Boulder, Colorado, USA
[2]Climate and Global Dynamics, National Center for Atmospheric Research, Boulder, Colorado, USA
[3]Atmospheric Chemistry Observations and Modeling, National Center for Atmospheric Research, Boulder, Colorado, USA

Key Points:

- Gravity wave distribution from lower atmosphere to upper thermosphere obtained from high-resolution WACCM-X
- Gravity wave forcing important for thermospheric circulation and composition
- Thermospheric/ionospheric disturbances driven by gravity waves quantified

Corresponding author: Han-Li Liu, `liuh@ucar.edu`

Abstract

A new version of NCAR Whole Atmosphere Community Climate Model with thermosphere/ionosphere extension (WACCM-X) has been developed. The main feature of this version is the species-dependent spectral element (SE) dynamical core, adapted from the standard version for the Community Atmosphere Model (CAM). The SE is on a quasi-uniform cubed sphere grid, eliminating the polar singularity and thus enabling simulations at high-resolutions. Molecular viscosity and diffusion in the horizontal direction are also included. The Conservative Semi-Lagrangian Multi-Tracer Transport Scheme (CSLAM) is employed for the species transport. An efficient regridding scheme based on the Earth System Modeling Framework (ESMF) is used to map fields between the physics mesh and geomagnetic grid. Simulations have been performed at coarse (∼200 km and 0.25 scale height) and high (∼25 km and 0.1 scale height) resolutions. The spatial distribution of the resolved gravity waves from the high-resolution simulations compare well with available observations in the middle and upper atmosphere. The forcing by the resolved gravity waves improves the wind climatology in the mesosphere and lower thermosphere in comparison to the coarse resolution simulations with parameterized forcing. It also impacts the thermospheric circulation and compositional structures, as well as thermospheric variablity. While larger scale waves are dominant energetically at most latitudes, smaller scale waves contribute significantly to the total momentum flux, especially at mid-high latitudes. The waves in the thermosphere are shown to be strongly modulated by the large-scale wind through Doppler shift and molecular damping, and they cause large neutral atmosphere and plasma perturbations.

Plain Language Summary

Small scale waves can be excited from daily weather near the Earth surface. These waves, termed gravity waves, can propagate upward and are thought to influence the middle and upper atmospheric regions. Such effects, however, are difficult to directly quantify by observations and numerical modeling due to their small scales and global presence. To address this challenge, we have developed a high-resolution whole atmosphere model (WACCM-X), which extends from the Earth surface to the upper thermsophere, that can partially resolve the small scale waves. The simulated waves are compared with available observations to verify the model results and to examine how these waves are distributed geographically and over altitudes. The forcing of these waves is found to be strong in the thermosphere. It affects the general circulation and the distribution of important atmospheric composition. The simulations also show that wave signatures can be clearly identified in the neutral and the ionized atmosphere, which can have important implications for space weather.

1 Introduction

The thermosphere and ionosphere (TI) system is the nexus of solar radiative and particulate, magnetospheric and lower atmospheric forcing, and affects the bottom-up and top-down coupling processes. As such, the compositional, thermal and dynamical structures of TI and its variation are a focal point of space environment and space weather research. The profound and complex variation of the whole TI system and its interactions with the magnetosphere during solar and geomagnetic storms is of key interests for space weather, and is a central theme of the NASA Diversity, Realize, Integrate, Venture, Educate (DRIVE) Center: the Center for Geospace Storms (CGS) (`https://cgs.jhuapl.edu/`). Meteorological and lower atmosphere forcing have also been shown to affect the TI on weather scales (H.-L. Liu, 2016, and references therein), as well as the TI responses during storm time (Pedatella & Liu, 2018). The lower atmosphere can also affect the TI system from subseasonal-to-seasonal scales (Gasperini et al., 2017, 2020; Richter et al., 2022) to variations associated with anthropogenic climate change (Roble

& Dickinson, 1989; Emmert et al., 2004, 2008; Solomon et al., 2018). The variability in the coupled TI system strongly influences the operation of Low-Earth Orbiting (LEO) satellites and space station, GPS navigation and radio communication. The dynamics of the middle atmosphere and TI determines the upward transport and escape of atomic hydrogen (Catling & Kasting, 2017; Jones Jr. et al., 2020) and downward transport of NO_x (Randall et al., 2006, 2009), which are species important for the long-term evolution of the Earth atmosphere and the climate variability of the middle and lower atmosphere, respectively.

Mesoscale processes, in particular atmospheric gravity waves (GWs), are thought to play an important role in coupling of the lower atmosphere with the space environment. While GWs are increasingly damped by the strong molecular viscosity in the thermosphere, waves with large vertical propagating speed can still penetrate to high altitudes (Pitteway & Hines, 1963). This is evidenced in observational studies relating TEC perturbations to strong tropospheric deep convective storms (e.g. Nishioka et al., 2013; Azeem et al., 2015, 2018). Limited satellite observations have shed light on the distribution and seasonal variation of GWs around 250 km, though it is not clear how they are related to the sources in the lower atmosphere (Park et al., 2014; Forbes et al., 2016; H. Liu et al., 2017). For the ionosphere, GWs can induce traveling ionospheric disturbances (TIDs), and there have been decades of study on their role in seeding ionospheric irregularities (e.g. Huang & Kelley, 1996a, 1996b; Hysell et al., 1990; Krall et al., 2013; Kelley et al., 1981; McClure et al., 1998; Retterer & Roddy, 2014). In recent years, theoretical and high-resolution numerical simulations have advanced our understanding of the GWs in the thermosphere. Secondary GWs from the dissipation of primary GWs can have large spatial scales and fast propagating speeds, and can thus play an important role in the upper atmosphere dynamics (Vadas & Fritts, 2001; Vadas, 2007; Vadas & Liu, 2013; Vadas & Becker, 2019; Becker & Vadas, 2020). It is also demonstrated that GWs can indeed seed equatorial plasma bubbles (EPBs) (Huba & Liu, 2020).

The need to understand the TI system in the context of its interactions with the lower atmosphere has motivated the development of numerical models spanning the whole atmosphere region, from Earth surface to the upper thermosphere, that can simulate the radiative, chemical, dynamical, and electrodynamical processes. A review of whole atmosphere modeling was given by Akmaev (2011), and model capabilities have advanced further since then, including enhanced thermospheric and ionospheric physics (Jin et al., 2011; Verronen et al., 2016; H.-L. Liu et al., 2018; Borchert et al., 2019; Wu et al., 2021) and whole atmosphere data assimilation (Wang et al., 2011; Pedatella, Raeder, et al., 2014; Pedatella et al., 2020). It has been recognized, however, that one of the major sources of bias in whole atmosphere models is the uncertainties associated with the parameterization of GW effects on forcing and transport (Pedatella, Fuller-Rowell, et al., 2014), which are necessitated by the limited model resolution. The poor model resolution also limit the whole atmosphere capabilities in resolving other TI effects by GWs (e.g. TIDs and ionospheric dynamo), and mesoscale processes in general. This need, along with the improved numerical algorithms and increasing computational power, has motivated and enabled the development of the high-resolution capability of whole atmosphere models (Watanabe & Miyahara, 2009; H.-L. Liu et al., 2014; Miyoshi et al., 2018; Becker & Vadas, 2018; Becker et al., 2022; Okui et al., 2022).

In the current study, we have developed the high resolution capability for the NCAR Whole Atmosphere Community Climate Model with thermosphere/ionosphere extension (WACCM-X), which makes it possible to resolve the meso-α range (200–2000km). With the model capability in solving interactive chemistry, transport, and ionospheric electrodynamics, we will examine the GW distribution and variation from the lower atmosphere to the upper thermosphere, the wave effects on the thermospheric circulation and composition, the scale dependence of wave contribution to the energy and momentum budget, and TI perturbations caused by the waves.

2 Model Description

WACCM-X is one of the atmosphere components in the NCAR Community Earth System Model (CESM). The thermospheric and ionospheric physics of WACCM-X is described in H.-L. Liu et al. (2018). The lower and middle atmosphere physics packages used in WACCM-X have recently been updated to WACCM version 6 (WACCM6) (Gettelman et al., 2019). Earlier versions of WACCM-X have been using finite volume dynamical core on a traditional latitude and longitude grid. One disadvantage of the latitude-longitude grid is the polar singularity: the size of the grid decreases toward 0 when approaching the pole. Polar filtering or smoothing has to be applied to maintain numerical stability, which affects the fidelity of the physics in the polar region and degrades the model performance at higher spatial resolutions. A new dynamical core option in CESM atmosphere components is the spectral element (SE) core, which employs a quasi-uniform cubed sphere grid (Lauritzen et al., 2018). This addresses the polar singularity issue, and enables simulations at much higher horizontal resolutions. The high-resolution capability of the SE dynamical core and its ability to resolve gravity waves was demonstrated in an experimental version of WACCM with specified chemistry (up to $\sim$140 km) (H.-L. Liu et al., 2014).

The SE dynamical core has recently been adapted for WACCM-X, by taking into consideration the species-dependence of mean molecular weight, dry air gas constant, and specific heats, which are necessary to properly resolve the thermosphere dynamics. Formulations of the these quantities used are described in H.-L. Liu et al. (2018), and similar formulations are used here. It is noted that in the SE dynamical core, the thermodynamics quantity used is temperature, not potential temperature. There is thus no need to correct for variable κ (the ratio between gas constant R and specific heat at constant pressure c_p). The implementation of species dependent thermodynamics uses the generalized thermodynamic infrastructure for moist air containing any number of forms of water (Lauritzen et al., 2018). This infrastructure has been extended to species dependent dry air so that the user specifies the major species via name list and the model automatically adapts. The details are given in Appendix A.

In addition to the modifications of the dynamical core thermodynamics, molecular viscosity and thermal conductivity (which previously only has been represented in the physics package in the vertical) is now also represented in the horizontal in the SE dynamical core. The formal equations are given in Appendix B. Again we highlight that similarly to the thermodynamic infrastructure, the molecular viscosity and thermal conductivity coefficients are computed by a common module shared between physics and dynamics to ensure consistency and flexibility. In additional to the physical damping, artificial viscosity needs to be applied to maintain numerical stability, as noted in the Appendix C. This artificially damps gravity waves, and the simulated waves discussed in the paper are therefore likely to be weaker than reality.

For uniform resolution applications the NCAR SE dynamical core has the option to use an accelerated transport scheme called CSLAM (Lauritzen et al., 2017, Conservative Semi-Larangian Multi-tracer scheme) and coupling to physics using a finite-volume physics grid (Herrington, Lauritzen, Taylor, et al., 2019; Herrington, Lauritzen, Reed, et al., 2019). This option provides more accurate and efficient (if enough tracers as is the case for WACCM-X) tracer transport and the use of a finite-volume physics grid alleviates spurious noise near element corners/edges (Herrington, Lauritzen, Taylor, et al., 2019).

In WACCM-X the ionospheric electric dynamo is computed in a modified magnetic apex coordinate system (H.-L. Liu et al., 2018; Richmond, 1995). The F-region O^+ transport equation is solved on its own latitude and longitude grid. It is thus necessary to perform efficient run-time communications for state variables among different grids. This is achieved via Earth System Modeling Framework (ESMF, Theurich et al., 2016, `https://`

`earthsystemmodeling.org/`) regridding operations. The WACCM-X data originate in the atmospheric physics layer of CESM and an unstructured ESMF mesh is created from the normally column-based physics by reading in a pre-computed ESMF mesh file. This allows all physics fields to be treated as gridded data. The dynamo and ion transport grids are rectangular (geomagnetic and geographic latitude/longitude, respectively) and ESMF objects for those are created dynamically at model initialization time. The dynamo grid is recreated yearly to account for changes in the geomagnetic main field. ESMF regridding operations are then used to transmit data between these grids.

Two model configurations are used for this study. For the high-resolution simulations, the horizontal configuration of the cubed sphere is NE120, corresponding to a quasi-uniform resolution of $\sim$25 km. The vertical resolution is 0.1 scale height in most of the middle and upper atmosphere. In the top 3 scale heights, the vertical resolution transitions to 0.25 scale height, because most of the waves with short vertical wavelengths are gone due to strong molecular damping. There are a total of 273 levels (L273). As a comparison, WACCM-X simulations have also been performed with NE16 horizontal resolution ($\sim$200 km) and 0.25 scale height vertical resolution for the middle and upper atmosphere (130 levels, L130). For both configurations, the model top is at 4×10^{-10} hPa ($\sim$600 km). The solar radio flux at 10.7 cm, a proxy used to parameterize solar extreme ultraviolet (EUV) irradiance, is set to 120 solar flux unit (SFU). The geomagnetic index Kp, used to drive Heelis empirical model for high latitude electric potential specification, is set to 0.33. Gravity wave parameterization scheme (Gettelman et al., 2019, and references therein) is used in the WACCM-X NE16/L130 simulations, but is turned off in WACCM-X NE120/L273.

3 Results

3.1 Distribution of Resolved Gravity Waves

Gravity wave activity level in the high resolution simulations is quantified as follows: neutral and ionospheric quantities, such as winds and temperature, electron density and total electron content (TEC), are first high-pass filtered in the zonal direction, retaining perturbations with zonal scales less than 2000 km. The standard deviation of these quantities are then computed in $2.5^\circ\times2.5^\circ$ latitude/longitude bins for each output time step. The standard deviation is used in this study to characterize the longitude, latitude, altitude and time dependence of the gravity wave activity.

Figure 1 shows the zonally averaged standard deviation of zonal, meridional and vertical winds and temperature for January. It is first noted that in the stratosphere, mesosphere and lower thermosphere the latitude/height distribution show the same morphology as previous observational studies (e.g., Ern et al., 2011; John & Kumar, 2012; Ern et al., 2018; Geller et al., 2013): (1) the winter hemisphere maximum is located at higher latitudes (50-60°N); (2) the summer hemisphere maximum is located at $\sim$20°S in the stratosphere and lower mesosphere, and shifts to higher latitudes above, coinciding with the large eastward wind shear. These features are also well captured in high-resolution WACCM simulations (H.-L. Liu et al., 2014; H.-L. Liu, 2016).

The standard deviations of zonal and meridional winds have similar latitude/height structure and similar magnitude. In the winter hemisphere (NH), their maximum values (20–30ms^{-1}) extend from the middle to high latitudes and 100–200 km, while in the summer hemisphere (SH) their maximum values are at mid-latitudes and located in the mesosphere and lower thermosphere (MLT) region. This difference is caused by the hemispheric/seasonal dependence of the molecular damping, which depends sensitively on the thermosphere temperature and is thus stronger in the summer hemisphere.

The maximum values of the vertical wind standard deviation, $\sim$10ms^{-1}, are also found at middle and high latitudes, but at higher altitudes than the horizontal winds (around 300km). This is likely due to the dominance of higher frequency gravity waves at higher altitudes, because only waves with the largest vertical propagating speeds and longest vertical wavelengths can survive the molecular damping. Furthermore, the buoyancy frequency increases with altitude. Since the ratio of the vertical and horizontal wind perturbations is approximately proportional to the ratio between wave frequency and buoyancy frequency according to the polarization relation, vertical wind perturbations at upper thermosphere can grow further with altitude even when the horizontal wind perturbations start to decrease.

The temperature perturbations have the maximum standard deviation values (up to 30 K) spanning 100 and 200 km in NH, and at around ∼150 km in SH. These large values are again located at middle to high latitudes.

The longitude/latitude dependence of temperature perturbations, averaged over 4 universal times (0, 6, 12 and 18 hours), are shown in Figure 2 for 4 levels (78, 1, 10^{-4}, and 10^{-7} hPa, corresponding to approximately the tropopause, stratosphere/stratopause, lower thermosphere, and upper thermosphere). At the tropopause height, strong activities are seen over major mountain ranges and plateaus, and over the Western Pacific warm pool. The distribution changes with altitude. For example, the strong orographic waves in both hemispheres disappear or are much weakened. In the summer/southern hemisphere, the zonal wind reversal at the tropopause and lower stratosphere form critical layers for the orographic gravity waves. Although the zonal mean zonal wind in the winter/northern statosphere and mesosphere is eastward, mid-latitude large-scale zonal wind at a specific longitude can be westward or 0 associated with the quasi-stationary planetary wave. For example, at ∼35°N the westward tilting easterly (westward wind) phase in the stratosphere and mesosphere extends across almost the entire latitude circle except between 60-95°W. As such, orographic gravity waves over Tibetan plateau and the Rocky Mountains are removed by critical layer filtering.

By comparing the standard deviation values at 1 and 78 hPa, it is seen that the wave activities over the Western Pacific is still prominent (over 3 K), but the peak has shifted southward by about 10° latitude. There is actually a band of activities centered around 20°S, with large standard deviation values (2-3 K) over the Central Pacific, Western South Atlantic/East Coast of Brazil, and Western Indian Ocean/Madagascar. These are likely convectively generated gravity waves that propagate southward. In the winter/north hemisphere, large activities are found poleward of 45°N, where the large-scale zonal wind are predominantly eastward at all longitudes. Peak standard deviation values extend from the eastern part of North America, across the north Atlantic, to western Europe, with magnitude of over 3K. Activities are also strong (>2 K) over the rest of Eurasia poleward of 45°N. By comparing to the stream function of the flow at that level, it is seen that these large activity regions correspond to the strongest eastward stratospheric jet as well as its exit region. The longitude and latitude distribution of wave activities in both hemispheres is in good agreement with the stratospheric gravity waves during January obtained from SABER measurements (Ern et al., 2011).

In the lower thermosphere, the large activities in the winter/northern hemisphere are still located at high latitudes, and the band of activities in the summer/southern hemisphere shifts further southward (as also seen in Figure 1), peaking at around 45°S. The time averaged longitude dependence of the wave activity in the NH is similar to that at the stratosphere, with peak values (over 10 K) extending from eastern North America to central Eurasia. The spatial distribution appears to be more uniform in comparison with the stratosphere. This results from both the horizontal propagation of the waves, and stronger time dependence due to tidal waves (and the time averaging) as will be discussed later. An equatorial band is also seen at the lower thermosphere, with magnitude up to ∼6 K. These waves may originate from relatively weak convective activities in the troposphere. They become more prominent and distinguished at the lower thermosphere resulting from amplitude growth and dispersion of the waves propagating in the meridional direction.

In the upper thermosphere, the longitude dependence of the time averaged wave activity in the NH display a pattern similar to that in the lower thermosphere, with large values (up to 12 K) from eastern North America to central Eurasia between 45°–60°N. The SH activity band shifts further southward, centered around 55°S, with magnitude (5 K) smaller than the NH due to stronger molecular damping. However, the maximum standard deviation values in both hemisphere are found near the geomagnetic poles, with values up to 17 K in the NH and 13 K in the SH. This is consistent with the thermospheric wave distribution obtained from CHAMP and GOCE measurements (Park et al., 2014; H. Liu et al., 2017). The corresponding maximum standard deviation of zonal wind perturbations at these locations have similar values to that of the temperature perturbations (17/13 K in NH and SH), which are comparable to the values from GOCE (H. Liu et al., 2017) (square amplitude of 100 m^2s^{-2}). The two peaks are likely caused by the reduced ion drag, when the gravity wave phase lines become more aligned with the field lines.

Gravity waves at higher altitudes display strong local time dependence, in contrast to the stratosphere (Figure 3). This is associated with the increasingly strong tidal motion and day-night difference at higher altitudes. At 1.1×10^{-4} hPa, this is most clear in the NH at mid to high latitudes, with stronger activities around LT 18 hour and 6 hour, when the large-scale winds are eastward. Diurnal variation is more prominent in the upper thermosphere: strong activities are found around LT 9 hour in the NH and LT 6 hour in the SH. The large-scale winds at these times are westward and poleward, and the gravity waves propagation is opposite to the winds. This sensitive dependence on the wind direction is because of the large molecular damping. The molecular damping is inversely proportional to the square of the vertical wavelength. Because the vertical wavelength decreases when propagating in the same direction of the wind due to doppler shift, these waves are more severely damped than the ones that propagate against the wind. It is worth noting that the peak wave activities at different altitudes are not always co-located. This implies that the waves peaking at different altitudes may originate from different sources, different spectral portion of the wave sources, and/or secondary generation of gravity waves. The local time dependence also underscores the significance of large-scale wind modulation.

3.2 Gravity wave forcing and impact on thermospheric circulation, composition and variability

The zonal mean zonal and meridional forcings by gravity waves with zonal scales less than 2000 km are calculated from the vertical divergence of the vertical fluxes of zonal and meridional momentum, respectively (Figure 4). By comparing the zonal forcing with the zonal mean zonal wind, it is seen that the former is responsible for the zonal wind reversal in the MLT. Further, there is a clear hemispheric/seasonal asymmetry of the reversal, with the eastward summer reversal stronger and located at lower altitudes ($\sim$90 km) and the westward winter reversal weaker at higher altitudes (above 100 km). This differs from WACCM-X simulation results obtained using parameterized gravity wave forcing and is in better agreement with observations (Swinbank & Ortland, 2003; Stober et al., 2021). Above the primary zonal wind reversal, the zonal gravity wave forcing changes direction again (to westward/eastward in the summer/winter hemisphere) within a rather shallow region (between about 100–120 km). This results from the dissipation of gravity waves that filter through the primary wind reversal in the MLT. This feature was qualitatively captured by parameterized gravity wave forcing (H.-L. Liu & Roble, 2002; H.-L. Liu, 2007), and it is responsible for driving a return circulation (winter-to-summer) between the summer-to-winter circulations in the MLT and the upper thermosphere.

In the upper thermosphere, the predominant wind is westward/eastward in the summer/winter hemisphere and summer-to-winter in the meridional direction. This is driven primarily by the differential heating. The zonal mean zonal forcing by gravity waves is eastward in both hemisphere, and the maximum value in the winter hemisphere (over 100 $ms^{-1}d^{-1}$) is larger than that in the summer hemisphere ($\sim$50 $ms^{-1}d^{-1}$). They are located at mid to high latitudes and 200–300 km altitudes in both hemispheres. While the eastward forcing is opposite to the mean zonal wind in the summer thermosphere, it is in the same direction as that in the winter thermosphere. Recall that the gravity wave activities are the strongest in local morning (Figure 3, LT 9 hour in the NH and 6 hour in the SH), and propagate eastward relative to the large-scale wind. The dissipation of these waves produces a net eastward forcing. The dominance of the eastward waves in the upper atmosphere may arise from the anisotropy of the source spectrum and/or filtering by the wind system. In earlier parameterization studies, similar anisotropy (with stronger eastward waves) was found necessary to reproduce the hemispheric/seasonal asymmetry of the wind reversal level in the MLT (H.-L. Liu & Roble, 2002). The zonal mean meridional forcing becomes large in the thermosphere, with magnitudes and hemisphere and altitude distribution similar to the zonal forcing. The direction of the forcing is from winter to summer, against the summer-to-winter meridional circulation.

The zonal and meridional forcing by gravity waves have important implications for the thermospheric circulation. In the NH, the Coriolis force associated with the eastward forcing is equatorward, thus it partially offsets the westward forcing by large-scale waves (Figure 4, mainly from migrating tides) and tends to weaken the summer-to-winter circulation. This reinforces the effect by the meridional forcing. On the other hand, the equatorward Coriolis force associated with the eastward forcing in the SH tends to strengthen the summer-to-winter circulation, thus offsetting the effect by the meridonal forcing. By using NE16 as a reference, the zonal mean zonal wind at 200 km and 50–60°N from NE120 is eastward and faster by $\sim$15 ms^{-1}, which results in a southward Coriolis forcing of $\sim$150 $ms^{-1}d^{-1}$. This is comparable to the southward gravity wave forcing of 100 $ms^{-1}d^{-1}$. On the other hand, the zonal mean zonal wind at 200 km and 50–60°S from NE120 is westward and over 7 ms^{-1} slower, leading to a northward Coriolis forcing of $\sim$70 $ms^{-1}d^{-1}$. This is stronger than the southward gravity wave forcing (30-40 $ms^{-1}d^{-1}$) at that latitude range. This hemispheric difference in forcing is reflected in the hemispheric differences zonal mean meridional and vertical winds (Figure 5). The figure shows the averages around 60° latitudes in both hemispheres, where the gravity wave forcing in NE120 is strong. Both meridional and vertical winds are weaker in the NH and stronger in the SH above $\sim$200 km. It is noted that the gravity wave forcing in the MLT tends to enhance the summer to winter circulation. The thermospheric gravity wave forcing in the NH (winter) hemisphere therefore offsets the effect by the MLT waves.

The change of the meridional/vertical circulation affects the thermospheric compositional structures. In the winter thermosphere, the downward circulation tends to bring down the atomic oxygen (O) rich atmosphere and increase its mixing ratio. The slower circulation, due to the compounded effect of Coriolis force associated with eastward forcing and the opposing meridional forcing, therefore leads to the decrease of the O mixing ratio. On the other hand, the upward circulation in the summer thermosphere has the opposite effect (reduce O mixing ratio). The Coriolis force therefore tends to reduce the O mixing ratio, while the opposing meridonal forcing tends to increase the O mixing ratio. Figure 6 shows the zonal mean, column integrated O/N_2 (simply referred to as O/N_2 thereafter), a proxy often used for thermospheric composition in measurements (Strickland et al., 1995; Meier, 2021), from simulations with high and coarse resolutions. The O/N_2 from the coarse resolution simulation is generally larger than observations, especially at higher latitudes in the winter hemisphere. This ratio in the high resolution simulation shows an overall decrease, in better agreement with observations. The largest decrease in the winter hemisphere (from 2.5 to 1.6 in the polar region) is consistent with the compounded effect from both zonal and meridional gravity wave forcing. Despite the enhanced upward circulation in the SH, O/N_2 still decreases, albeit with a smaller magnitude than in the NH (by ~ 0.1). This is likely due to the enhanced effective diffusion by gravity waves (H.-L. Liu, 2021), which also tends to decrease O/N_2. As shown by Qian et al. (2009), adding eddy diffusion at the lower boundary of TIE-GCM could correct the overestimation O/N_2 in the model and achieve better agreement with TIMED/GUVI measurements. The high-resolution simulations therefore elucidate the processes by which gravity waves can affect the O/N_2, namely both circulation and diffusion. The improved agreement of O/N_2 also serves a validation of the resolved gravity waves.

The changes in the major species and the transport cause changes in minor species. For example, the global mean NO is larger in the high resolution simulation than that from the coarse resolution simulation above ∼70 km. The increase in the thermosphere is likely due to the larger abundance of N_2, and the increase in the mesosphere probably results from enhanced transport by the resolved waves (H.-L. Liu, 2021). Because of this NO increase, NO cooling rate also increases. For example, the peak NO cooling rate at 60°S and ∼130 km from the high resolution simulation is ∼35% larger than the coarse resolution simulation (Figure 7). Another important energetics quantity for the TI system is the Joule heating. The vertical profiles of Joule heating at the same location from the high and coarse resolution simulations are shown in the same figure. The peak value at ∼120 km from the high resolution simulation is ∼33% larger than the lower resolution results. The increase of Joule heating is likely due to the smaller scale variations in ion drifts and winds, which are important for producing Joule heating (Codrescu et al., 1995). As will be shown in Section 3.4, smaller scale perturbations of ion drifts are excited by gravity waves. The increases of the NO cooling and Joule heating in high resolution simulations are seen at all latitudes (Figure 7).

The mean circulation varies strongly from day to day. Figure 8 shows the zonal mean and daily averaged meridional and vertical winds at 60.5°N near 250 km from 13 to 31 January from both the high-resolution (solid) and coarse-resolution (dotted) simulations. The ranges of the meridional wind variation during this time period are similar between the two simulations (10–18 ms^{-1}), but the day-to-day variation is stronger in the high-resolution simulation. The difference in day-to-day variation of the mean vertical wind is more significant: between 0 and -0.8 ms^{-1} in the high-resolution simulation and -0.35 and -0.55 ms^{-1} in the coarse-resolution simulation. The large day-to-day variability of the circulation results from the variability of the driving force by waves. This is demonstrated in Figure 9 by the mean zonal and meridional forcing by gravity waves (with zonal scales less than 2000 km). Both vary between 0 and 200 $ms^{-1}d^{-1}$.

Tides and tidal variability are affected by gravity waves. Figure 10 compares the mean and standard deviation of the amplitudes of three major tides (migrating diurnal (DW1) and semi-diurnal (SW2), and non-migrating diurnal, eastward propagating wavenumber 3 (DE3)) from the high-resolution and coarse resolution simulations. The latitude/height structures of the tides are similar from the simulations, and are consistent with their climatology. The amplitudes of DW1 and DW3 from the simulations are also comparable, while SW2 in the high-resolution simulation has larger amplitude, especially its peak value in the winter lower thermosphere. The standard deviation values of all three components, on the other hand, are larger throughout the middle and upper atmosphere in the high-resolution simulations.

3.3 Scale dependence of wave power and momentum flux

With the horizontal resolution of ∼25 km, the model can effectively resolve gravity waves with horizontal wavelengths longer than ∼200 km. The meso-β scales are poorly resolved or unresolved, but they can still have important contribution to the momentum budget up to the lower thermosphere (H.-L. Liu, 2019). Here we examine the scale dependence of the kinetic energy and momentum flux in the thermosphere and the contributions from waves of different scales using the same method proposed by H.-L. Liu (2019).

As shown in Figure 11, the zonal wavenumber power spectral density (PSD) of the zonal wind and spectra of vertical flux of zonal momentum still follow power-law in the thermosphere. It is also seen the transition from steeper slopes at large scales to shallow slopes at smaller scales occurs at larger wavenumbers (between 10 and 20) in the thermosphere. This indicates the relatively lower level of gravity wave activity, probably due to increasing molecular damping.

Figure 12 shows the contributions to the PSD of the zonal wind and the momentum flux spectrum within the zonal scale of 30–2000 km, by waves with zonal scales between 300–2000 km and 30–300 km. The waves within the scale ranges between 300 and 2000 km are fully resolved, while waves with scales less than 200 km are under- or unresolved. One of the considerations for looking at 30–300 km is that it is the measurement range of the upcoming NASA Atmospheric Waves Experiment (AWE) mission (Taylor et al., 2017). There are clear differences between the spectral compositions in the thermosphere ($>$ 100 km) and below, and between PSDs and momentum flux spectra. The larger scale waves are more prominent in the thermosphere, and they contribute more to PSDs due to their steeper spectral slopes. Between 100–300 km, waves with zonal scales between 300 and 2000 km contribute to over 75% of the total zonal kinetic energy (between 30 and 2000 km) at low and mid-latitudes, and down to 40% (NH) and 55% (SH) at high latitudes. Below 100 km the contribution can drop to 40% around 20°S and 20% at 40–50°N. The percentage contribution of this scale range to the momentum flux shows a similar spatial variation, but with lower values: 45-60% between 100–300 km and 40°S–40°N, and 15–50% at higher latitudes; below 100 km less than 10% at mid to high latitudes in both hemispheres and up to 60% over the equator. The percentage contributions by the 30-300 km are the residual of those by 300-2000 km, but they are shown in Figure 12 for clarity. In the middle atmosphere, waves from this scale range clearly play a dominant role, more than 90% over broad latitude regions in both hemispheres, and up to 60% over the equator. This dominance underscores the essential need for gravity wave parameterization in the stratosphere, mesosphere and lower thermosphere in coarse resolution models. The smaller scale contribution can still be large in the thermosphere, up to 80% at higher latitudes. It is noted that the percentage contribution by the smaller scale waves can be overestimated by this method, when the momentum flux spectrum is over flattened when the zonal wind become too large due to insufficient gravity wave forcing in the model (H.-L. Liu, 2019).

3.4 Neutral and plasma perturbations caused by gravity waves

As discussed in previous sections, gravity waves cause perturbations in neutral winds and temperature in the thermosphere, and the perturbations show strong local time dependence. The wave structure in zonal wind and its dependence on local time can be clearly seen in Figure 13, with the zonal wind perturbations tilt eastward into the westward wind (local daytime) and westward into the eastward wind (local nighttime). This is most evident above ∼120 km and at all latitudes. Modulation of gravity waves by the migrating semi-diurnal tide (SW2) in the lower thermosphere (below ∼120 km) is seen at 50°N where SW2 is strong.

To better understand the wave effects in the thermosphere and ionosphere, we examine most closely the neutral and plasma perturbations near the F-region peak. A high-pass filter using the Savitzky-Golay method (Savitzky & Golay, 1964) is applied to neutral meridional wind, electron density, total electron content, and the zonal and vertical components of E×B drifts. Two period ranges are examined: shorter than 2 hours (0.14 mHz), and shorter than 20 minutes (0.83 mHz).

Figure 14(left) shows the neutral meridional wind perturbation in the F-region with period shorter than 2 hours. Clear wave signature is seen, with the largest amplitude (up to 80 ms^{-1}) found at mid to high latitudes in the winter hemisphere. The wave propagation direction has an evident local time dependence, with the propagation direction being generally opposite to the large-scale F-region wind. For example, the wind changes quickly from northeastward on the night side to northwestward on the day side around the terminator at mid-high northern latitudes. As such, the propagation direction of the gravity waves changes from southwestward on the night side to southeastward on the day side. Meridional wind perturbations with periods shorter than 20 min can still be quite strong at mid to high winter latitudes, up to 25 ms^{-1} (Figure 14, right). Their spatial distribution is similar to those shown in left figure, and the spatial scales are generally smaller.

Figure 15 (left panel) are the electron density perturbations (relative to the unfiltered value) near the F-region peak with periods less than 2 hours and less than 20 minutes. The spatial distribution and local time dependence of the perturbations and their propagation are very similar to gravity wave signatures seen in the meridional wind (Figure 14), suggesting the gravity waves as the main driver of these traveling ionospheric disturbances (TIDs). The relative perturbation amplitude associated with the waves is about $\pm 15\%$ (< 2 hours) and $\pm 5\%$ (< 20 min). Similar features are also seen in the total electron content (TEC) (Figure 15 right panel), with magnitudes of $\sim \pm 3\%$ (< 2 hours) and $\sim \pm 1\%$ (< 20 min). It is also worth noting that the consistent southwestward propagation of neutral wind perturbations and TIDs at night time suggests that gravity waves can provide an alternative mechanism to Perkins instability in driving this propagation pattern. The large relative changes around the terminators are artifacts from the filtering. An animation of the relative TEC perturbations (period less than 2 hours) from one day of simulation (January 13) has been included as Supporting Information (Movie S1).

Both wind and electron density perturbations are significant according to these simulations. The field aligned drift perturbation associated with the neutral wind would be of similar magnitude. It is noteworthy that the frequency range overlaps with that of ultra-low frequency (ULF) waves (Pc5-6, period shorter than 20 minutes). These gravity wave driven perturbations may thus play a role in magnetosphere, ionosphere and thermosphere coupling. This will be explored in the future using coupled geospace models, such as the Multiscale Atmosphere-Geospace Environment (MAGE) model (`https://cgs.jhuapl.edu/`).

Wave oscillations of wind and electron density (thus electric conductivities) perturb the E$\times$B drift (Figure 16). Both the zonal and vertical components of E$\times$B have the largest amplitudes around the geomagnetic equator, up to $\sim$5 ms^{-1} (< 2 hours), 1.5 ms^{-1} (zonal, < 20 min) and 0.8 ms^{-1} (vertical, < 20 min). The strongest perturbations are found during night time, probably because the high frequency wind perturbations are generally stronger in the F-region, and the F-region dynamo is dominant during nighttime. While the phase lines of the perturbations are perpendicular to the geomagnetic equator, they curve toward eastward or westward directions away from the equator, with a "C" or reverse "C" shape. This likely reflects the relative position of the wave phase lines of the wind perturbations with respect to the field lines. A more quantitative study will be conducted in the future.

4 Summary and Conclusions

With the newly developed species-dependent spectral element dynamical core, WACCM-X simulations can now be performed with high spatial resolution: $\sim$25 km horizontally and 0.1 scale height vertically. The high-resolution simulation for January has been analyzed to study the gravity wave distribution and the wave effects in the thermosphere and ionosphere. The overall wave activity continues to increase with altitude in the thermosphere, with horizontal wind and temperature perturbations maximizing between 110–200 km, and vertical wind between 200-300 km. The largest wave activities are located at higher latitudes, with larger magnitude in the northern (winter) hemisphere. In the winter hemisphere, the longitudinal distribution of gravity waves from the mesosphere to the upper thermosphere is similar to that in the stratosphere, with the strongest activities extending from eastern North America, across the North Atlantic and to western Eurasia. The winter stratospheric jet may play an important role in exciting these waves. In the summer hemisphere, the peak wave activities shift from tropical latitudes at lower altitudes to higher latitudes with increasing height up to the upper mesosphere, coincident with the altitudes with zonal wind reversal and/or the large eastward shear of the mean zonal wind. Gravity waves display strong local time dependence in the upper atmosphere due to the modulation by tidal waves and the large day-night change of large-scale atmosphere state. In particular, the thermospheric gravity waves propagate predominantly against the large-scale wind. These waves have larger intrinsic frequencies, vertical wavelengths and propagation speeds due to doppler shift, and are thus less vulnerable to the strong molecular damping. The strongest wave activities in the upper thermosphere are near magnetic poles in both hemisphere. This could be due to reduced ion drag for gravity waves with large vertical wavelengths, whose phase lines become more parallel with the fieldlines. The features of wave distribution are similar to available observations in the middle and upper atmosphere.

The dissipation of the gravity waves in the thermosphere leads to strong forcing in the zonal and meridional directions. In January, the mean zonal/meridional forcing is found to be predominantly eastward/southward in both hemispheres, with the largest values found at mid-high latitudes between 200–300 km (exceeding 100 $ms^{-1}d^{-1}$ in the NH). The Coriolis forcing associated with the eastward gravity wave forcing is equatorward. Therefore the zonal and meridional forcings both tend to slow down the mean meridional circulation in the NH, while in the SH they offset each other. The thermospheric circulation changes the compositional structure: the slowdown of meridional/downward circulation in the winter hemisphere reduces the column integrated O/N_2. This ratio is further reduced by wave induced transport. These changes result in improved agreement with observations. The gravity wave forcing, the mean circulation and the tides change significantly from day to day.

The zonal spectra of the kinetic energy and the vertical momentum flux still follow power-law distributions in the thermosphere. The spectral slopes of the latter is generally shallower than the former, as in the lower and middle atmosphere. The power-law distributions allow the examination of the scale dependence of kinetic energy and momentum flux. For kinetic energy, larger scale waves are dominant at most latitudes. For momentum flux, on the other hand, smaller scale waves can contribute significantly, especially at middle to high latitudes.

Gravity waves are an important driver of traveling atmosphere disturbances (TADs) and traveling ionosphere disturbances (TIDs). The waves and these disturbances depend sensitively on the background wind in the thermosphere, which is in turn local time dependent. This is because the molecular damping is inversely proportional to the square of the vertical wavelength, which changes as a result of Doppler shift by the background wind. The magnitude of the wave induced TID in TEC is $\sim$3% (periods $<$ 2 hours), with temporal and spatial structures similar to the F-region electron density perturbations and the gravity waves at F-region altitudes. Even with this hydrostatic model, the simulated thermospheric and ionospheric perturbations still have significant power at short periods (less than 20 min). Its role in magnetosphere-ionosphere-thermosphere coupling is worth further investigation in future studies.

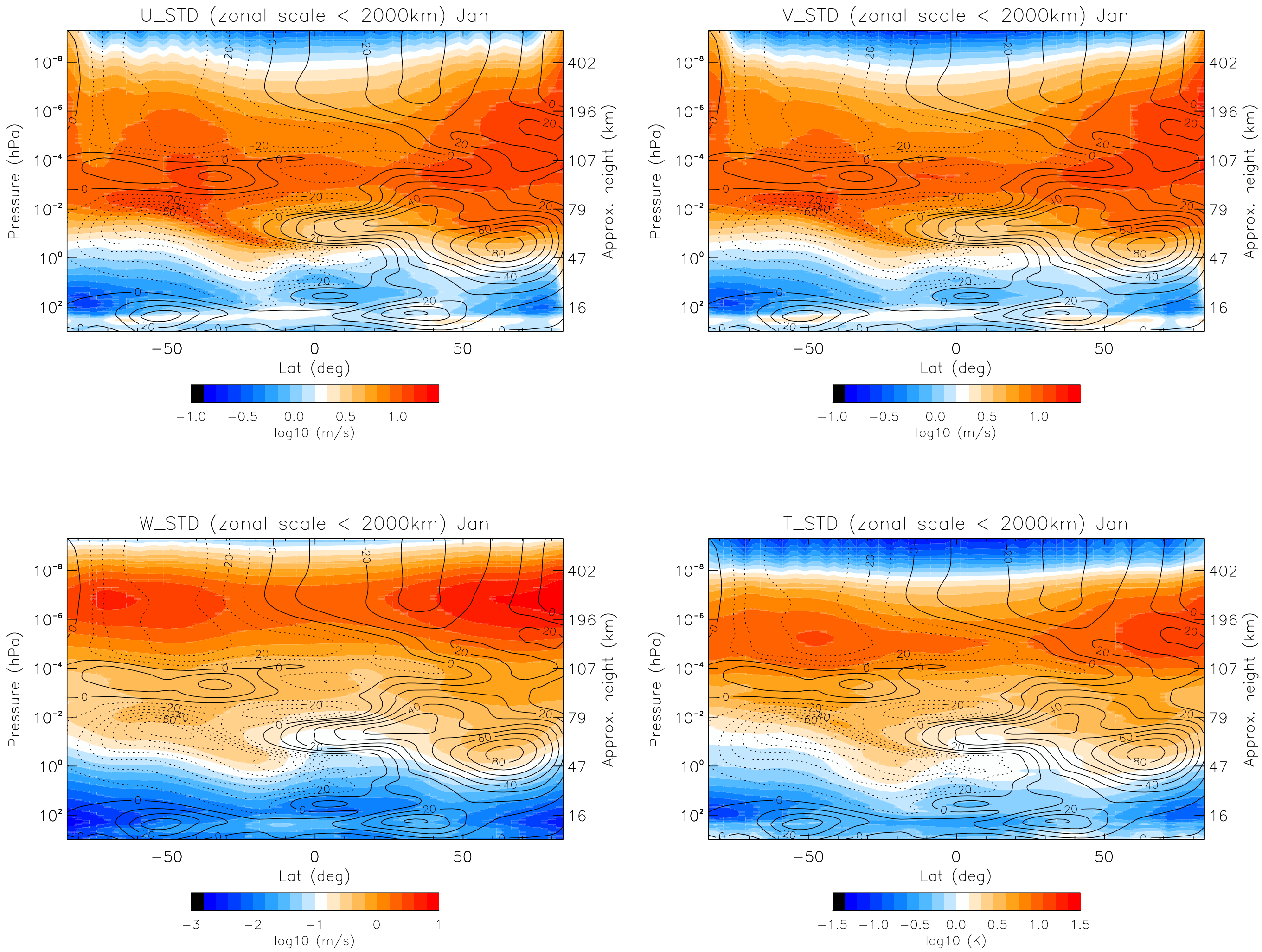

Figure 1: Zonally averaged standard deviation of (upper left) zonal, (upper right) meridional, (lower left) vertical winds and (lower right) neutral temperature perturbations with zonal scales less than 2000 km for January. Contour lines are zonal mean zonal wind (Solid: eastward, with contour interval of 10 ms^{-1}).

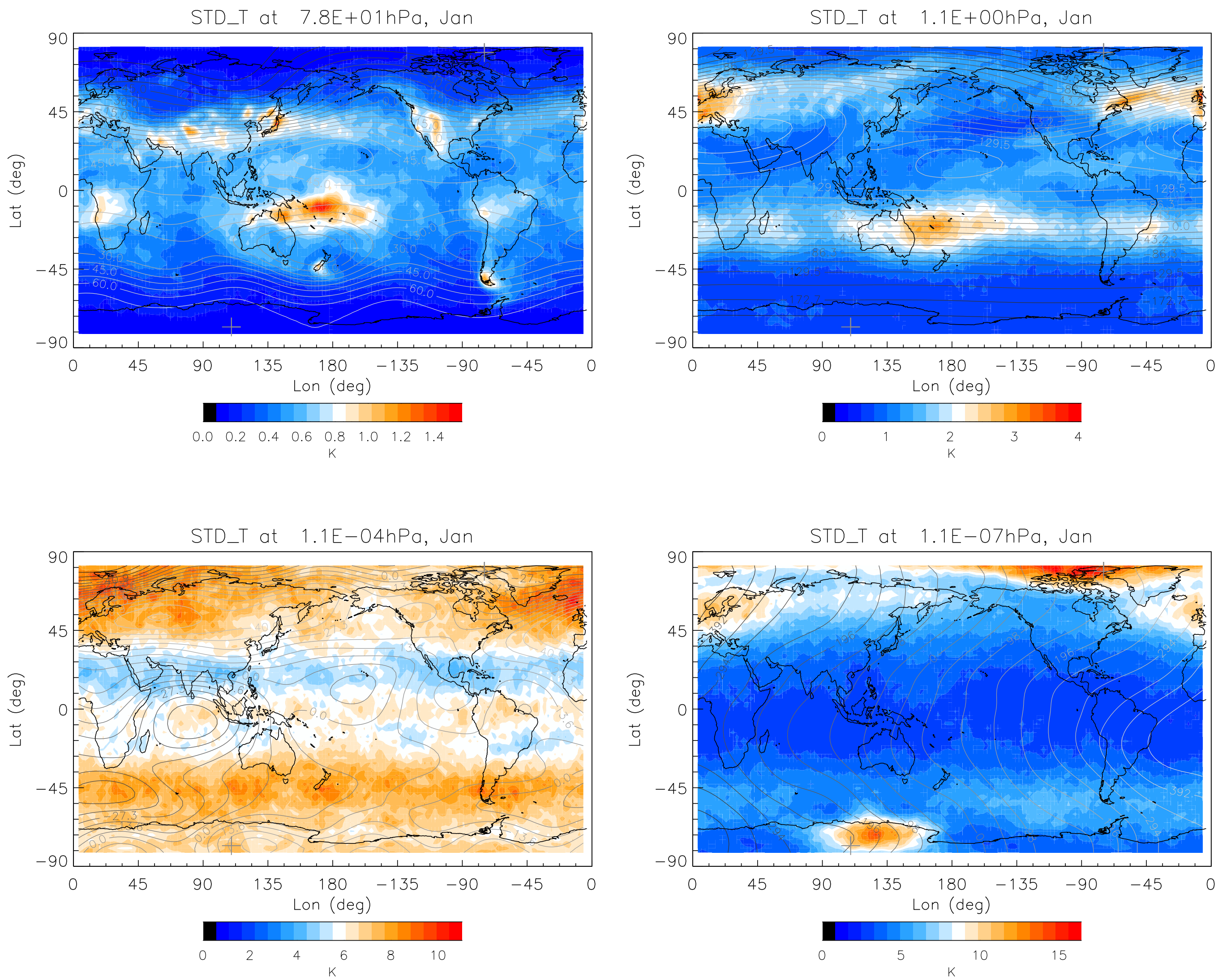

Figure 2: Standard deviation of temperature perturbations at (upper left) 78, (upper right) 1.1, (lower left) 1.1×10^{-4} and (lower right)1.1×10^{-7} hPa, averaged over four UT times (0, 6, 12, and 18 hours) for January. The contour lines are stream functions calculated from the horizontal winds. Contour lines with lighter shades have larger values. Atmosphere flow is toward the right of the down-gradient direction.

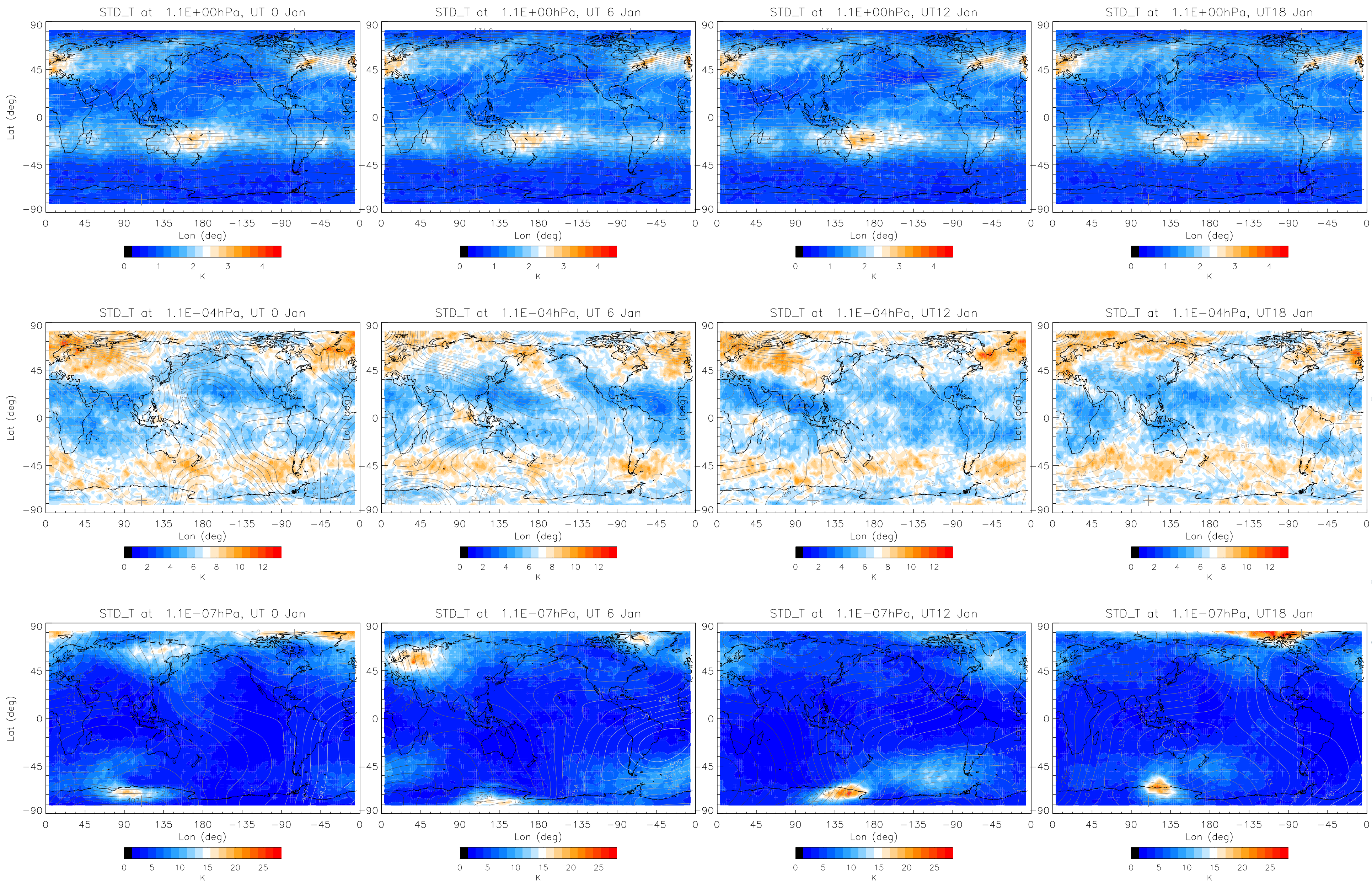

Figure 3: Standard deviation of temperature perturbations at (upper panels) 1.1, (middle panels) 1.1×10^{-4} and (lower panels) 1.1×10^{-7} hPa at four UT (0, 6, 12, and 18 hours, from left to right) for January. The contour lines are stream functions calculated from the horizontal winds. Contour lines with lighter shades have larger values. Atmosphere flow is toward the right of the down-gradient direction.

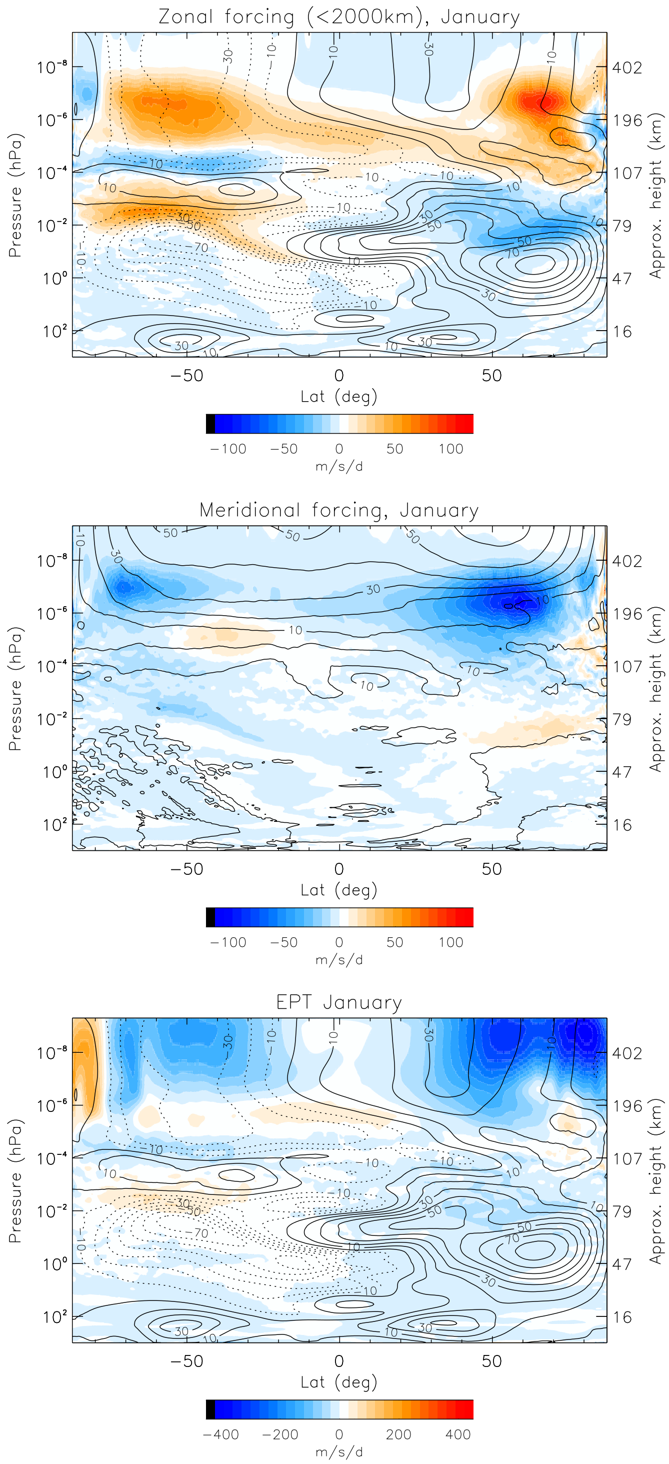

Figure 4: Zonal mean (upper panel) zonal forcing and (middle panel) meridional forcing by gravity waves with zonal scales less than 2000 km. Contour lines are zonal mean zonal wind in the upper panel (solid: eastward) and zonal mean meridional wind in the middle panel (solid: northward). Contour intervals: $10 ms^{-1}$. Lower panel: Total zonal mean zonal forcing by all resolved waves. Contour lines are the same as in the upper panel.

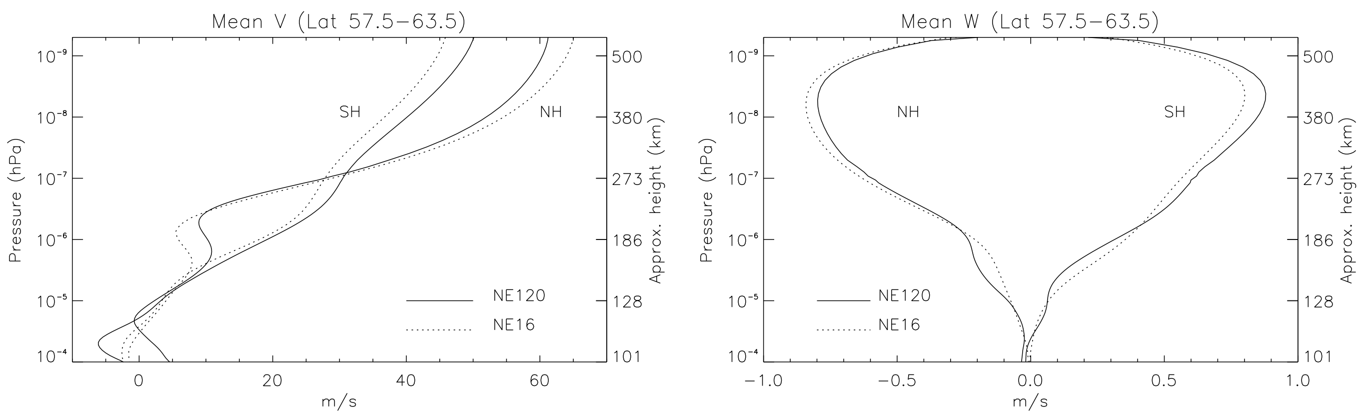

Figure 5: Zonal mean (left) meridional and (right) vertical winds in the thermosphere averaged over 57.5–63.5° latitudes in both hemispheres. The solid lines are from the high resolution simulation, while the dotted lines are from the coarse resolution simulation.

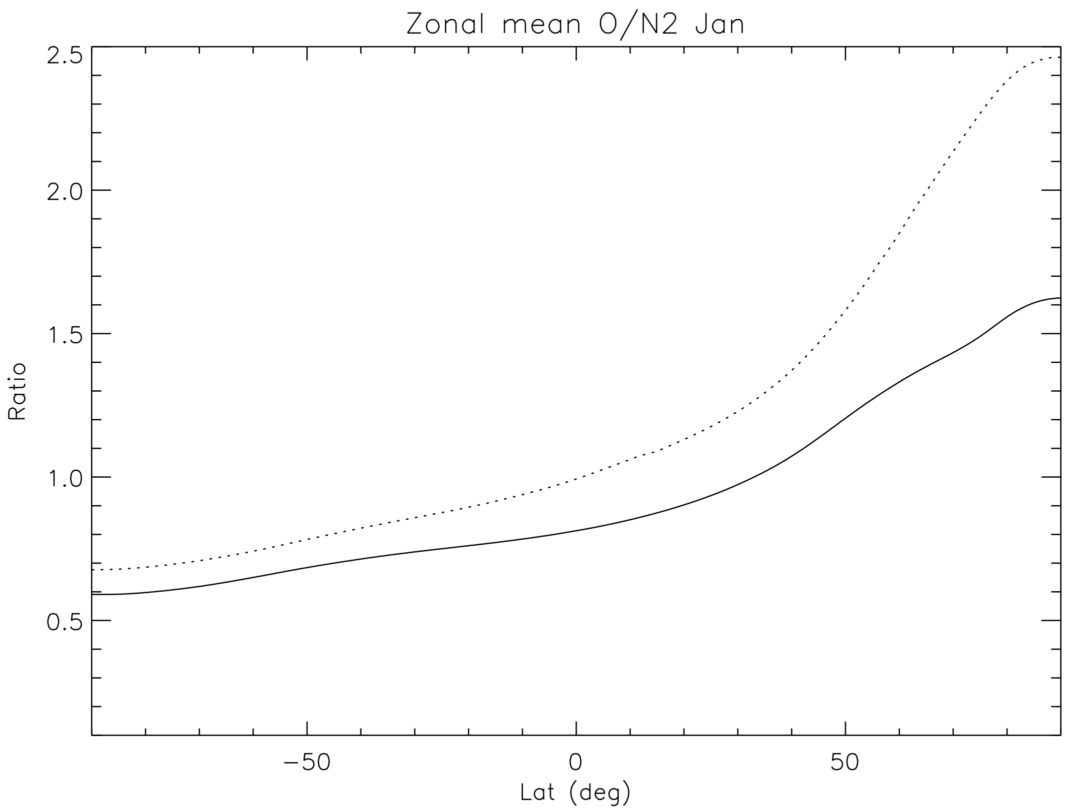

Figure 6: Zonally averaged O/N_2 (column integrated) from high resolution (solid) and coarse resolution (dotted) WACCM-X simulations.

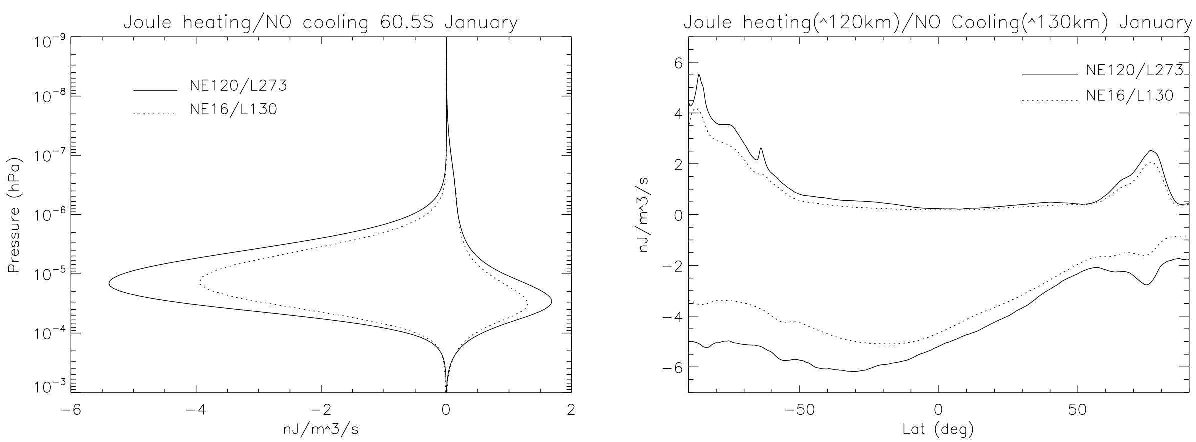

Figure 7: Vertical (left) and latitudinal (right) profiles of Joule heating and NO cooling from high-resolution (solid lines) and coarse-resolution (dotted lines) simulations.

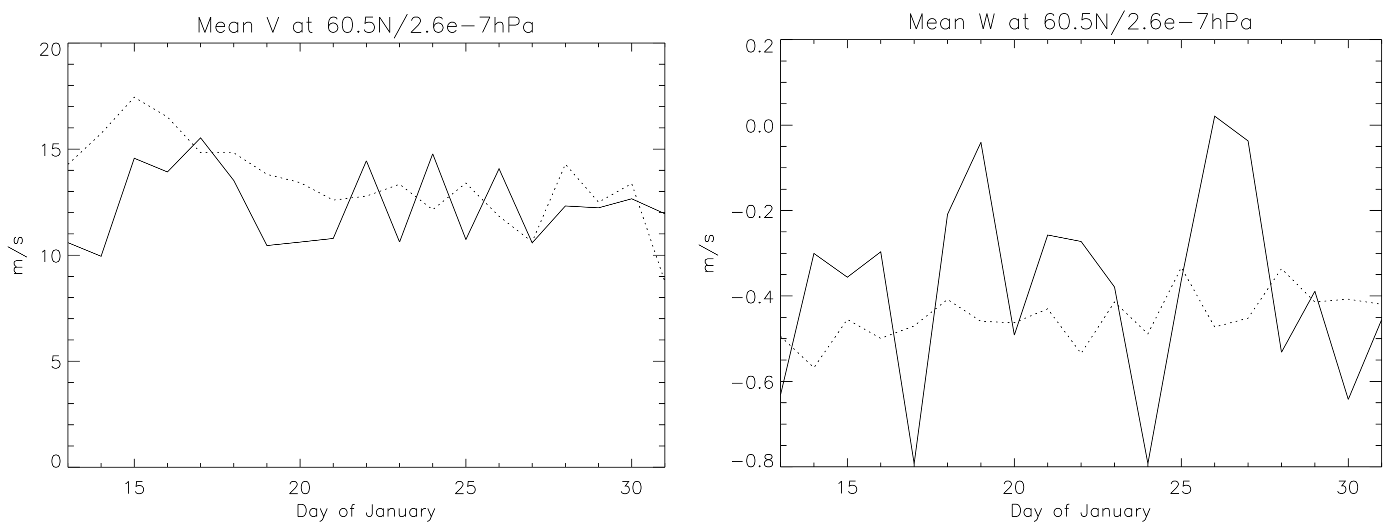

Figure 8: Zonal mean (left) meridional and (right) vertical winds at 60.5°N and 2.6×10^{-7} hPa for 13–31 January. Solid lines: high resolution simulation. Dotted lines: coarse resolution simulation.

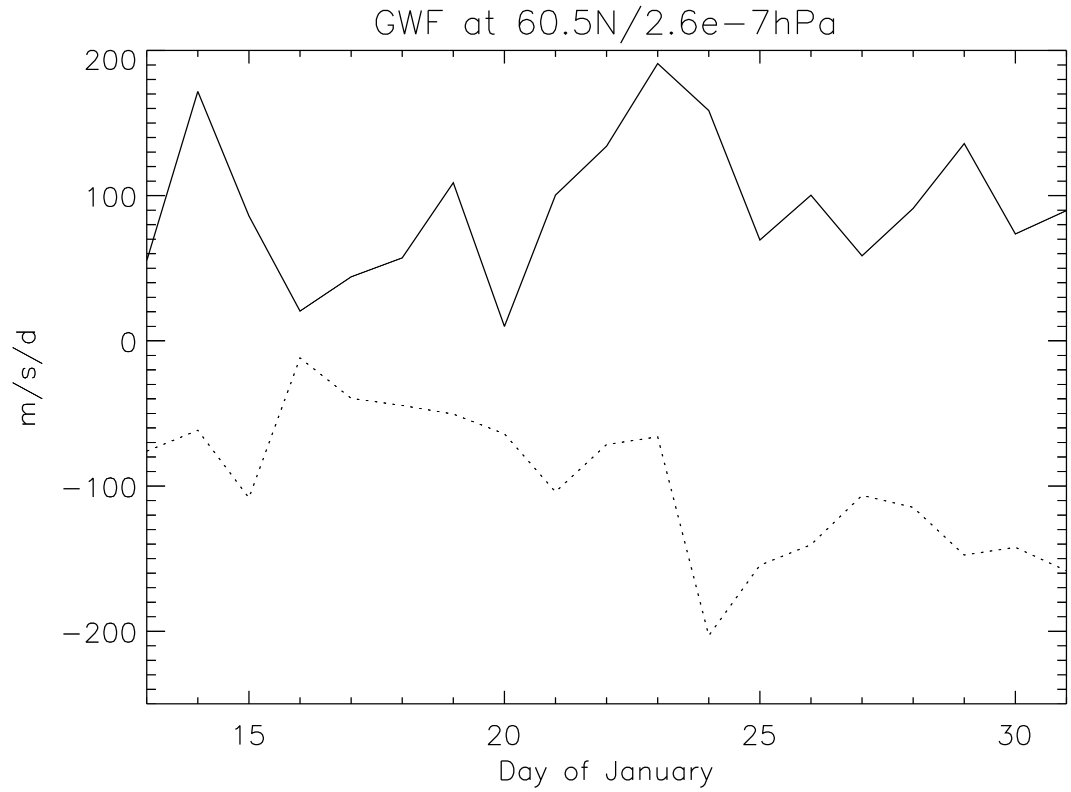

Figure 9: Zonal mean zonal (solid line) and meridional (dotted line) forcing at 60.5°N latitude and and 2.6×10^{-7} hPa for 13–31 January.

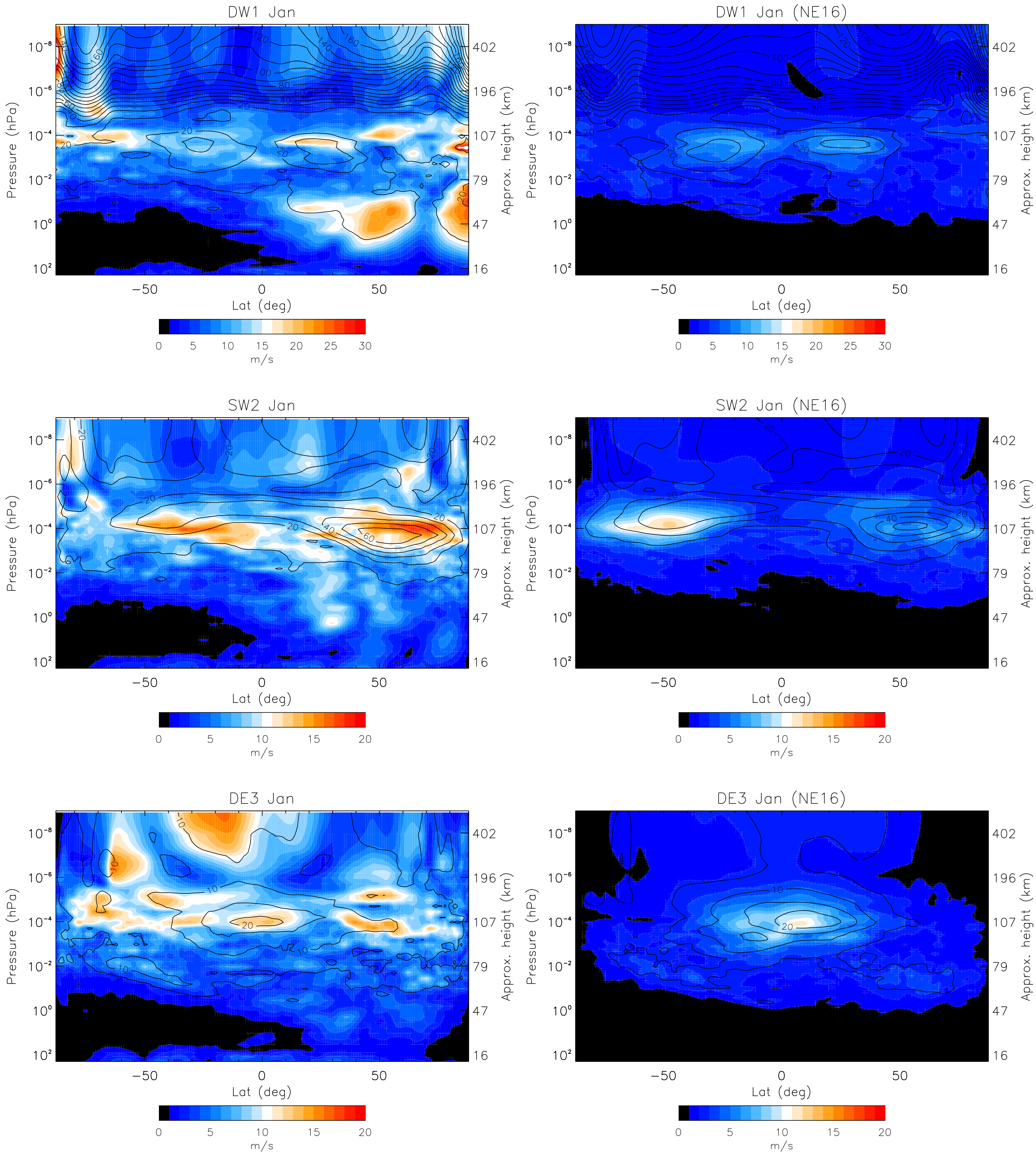

Figure 10: The mean (line contour) and standard deviation (color contour) of the DW1 (upper), SW2 (middle) and DE3 (lower) tidal components from the NE120 (left) and NE16 (right) simulations. Line contour intervals: 10ms^{-1} (upper and middle) and 5ms^{-1} (lower).

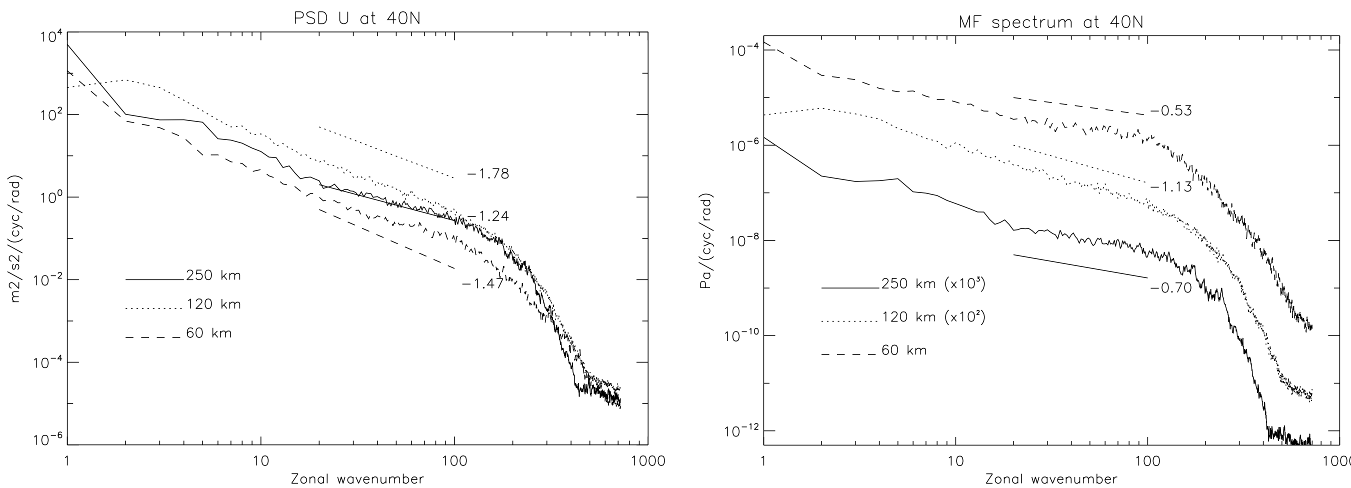

Figure 11: Zonal wind kinetic energy spectra (left) and momentum flux spectra (right) at 40°N and 3 different altitudes (60, 120 and 250 km). Spectral slopes for the mesoscale range (zonal wavenumber 20–100) are shown by the straight lines.

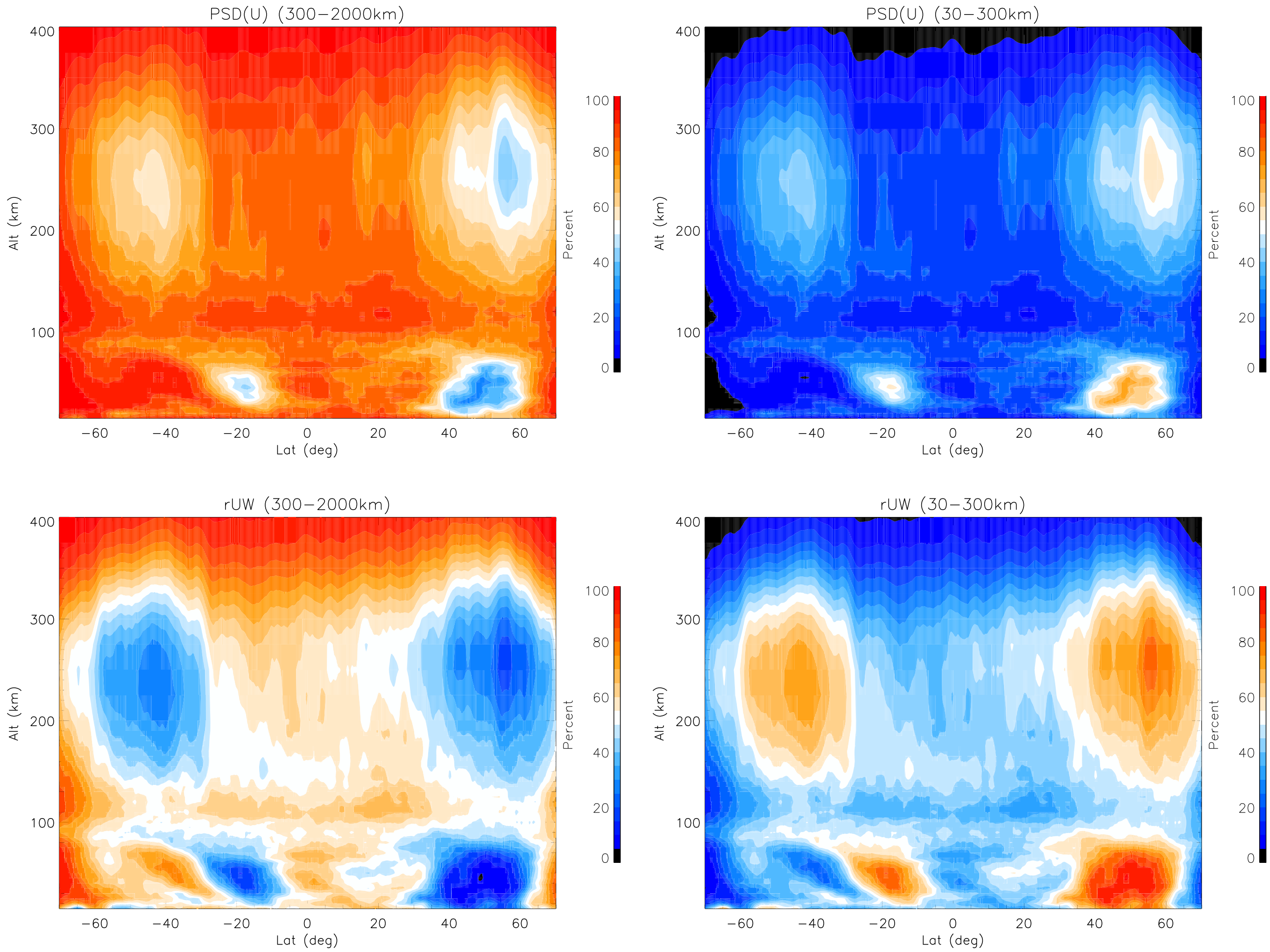

Figure 12: Percentage contributions to the total (upper panels) zonal kinetic energy and (lower panels) vertical flux of zonal momentum by (left panels) larger zonal scale waves and (right panels) smaller zonal scale waves.

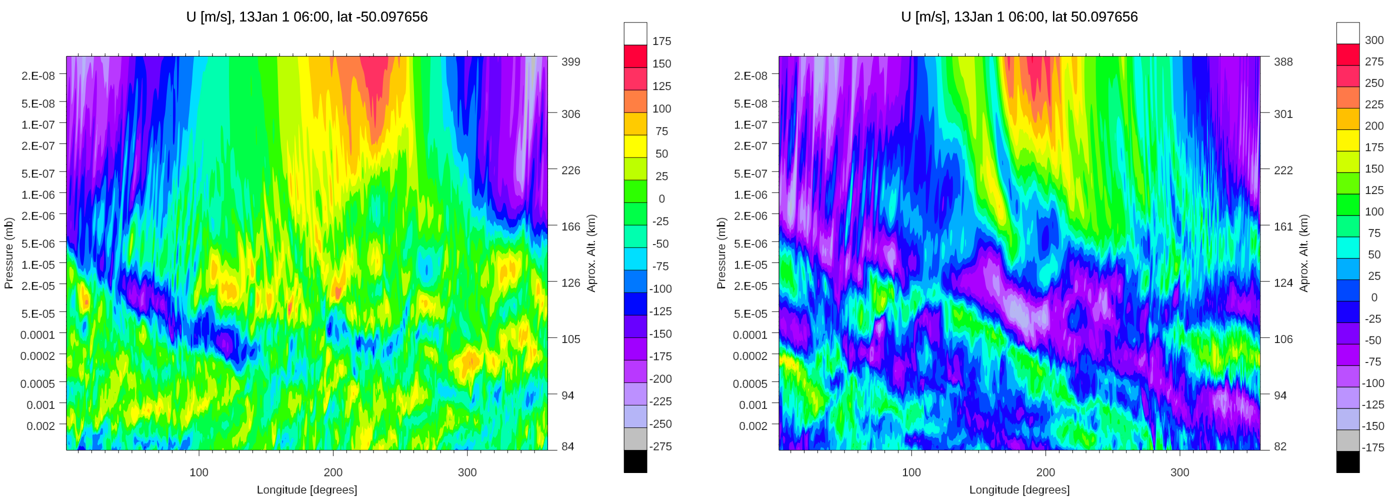

Figure 13: Upper mesosphere and thermosphere zonal wind at (left) 50°S and (right) 50°N and UT 6 hour on January 13.

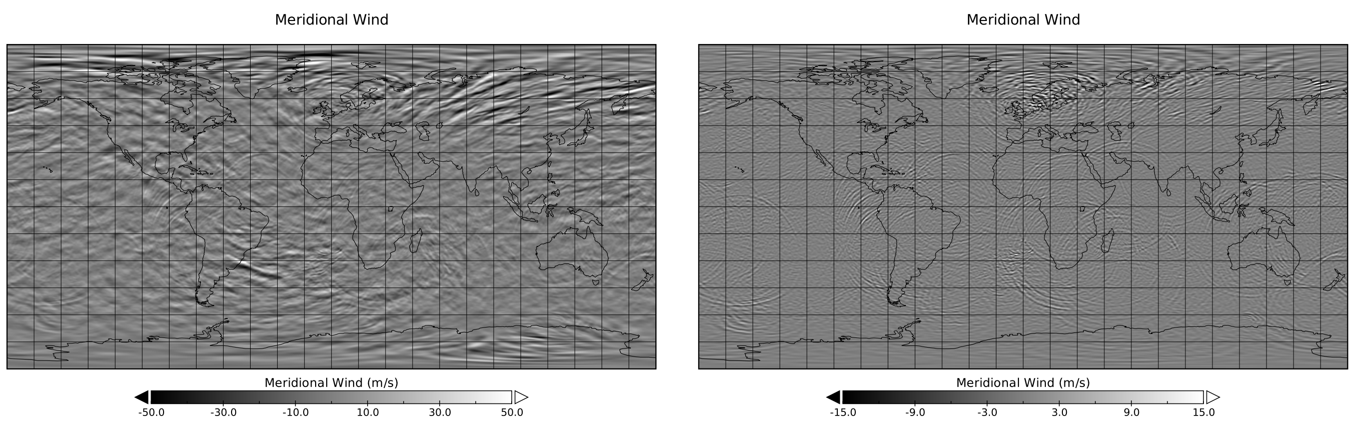

Figure 14: High-pass filtered meridional wind, with period shorter than (left panel) 2 hours and (right panel) 20 minutes. The UT time is 3 hour on January 30th.

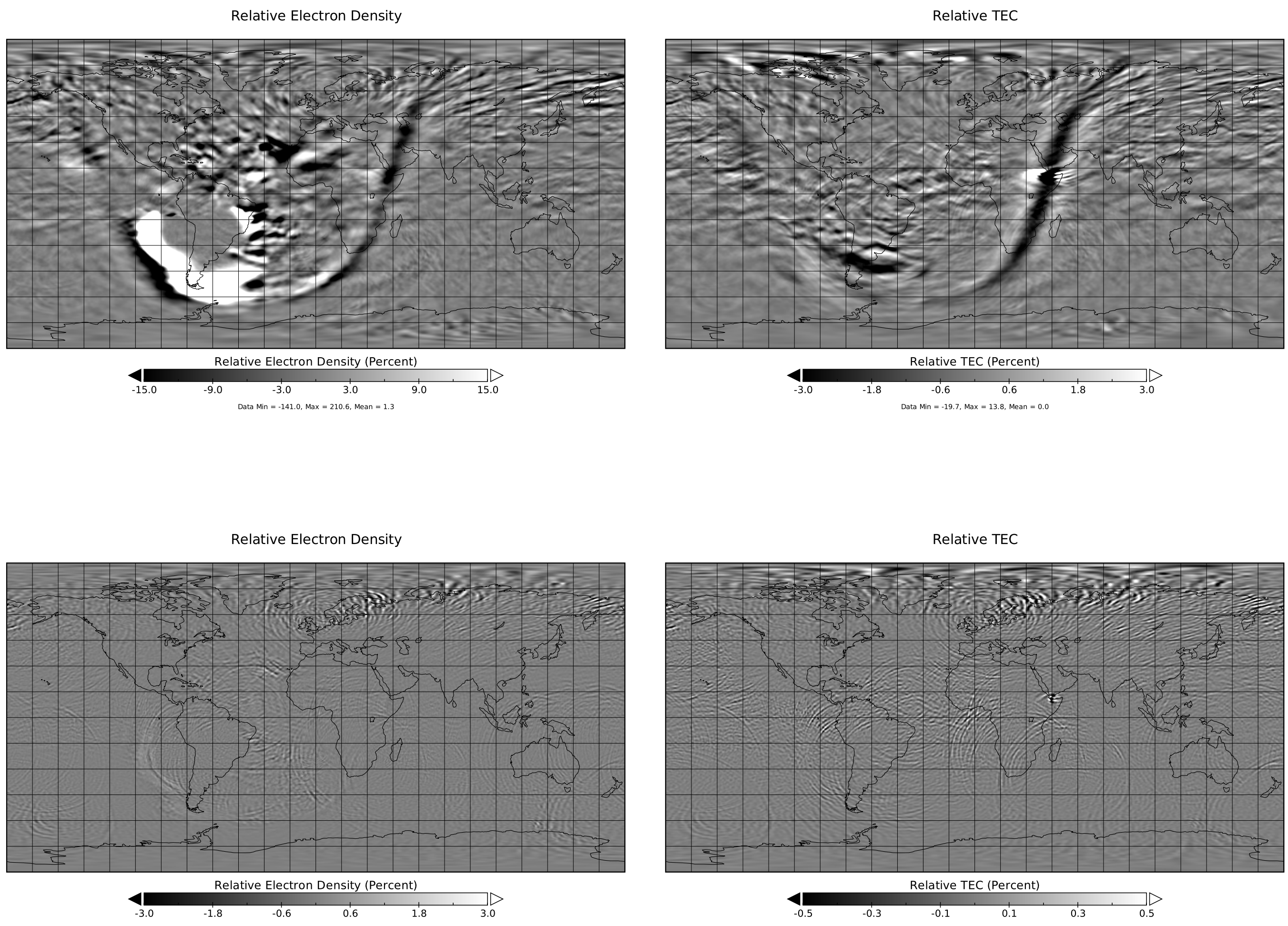

Figure 15: High-pass filtered (left panels) relative electron density perturbations near F region peak and (right panels) relative total electron content (TEC) perturbations, with period shorter than (upper panels) 2 hours and (lower panels) 20 minutes. The UT time is 3 hour on January 30th.

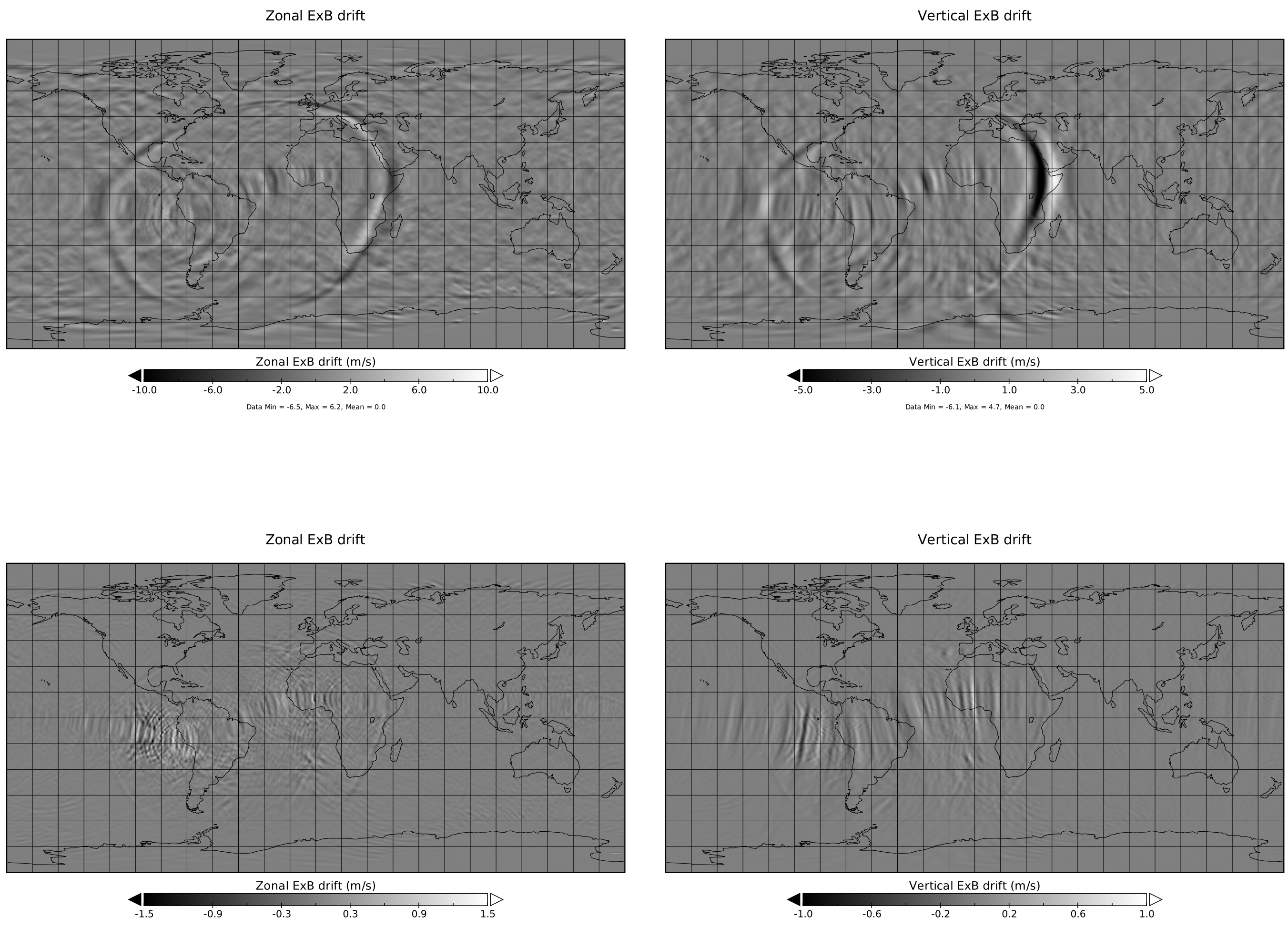

Figure 16: High-pass filtered (left panels) zonal and (right panels) vertical components of E×B drifts, with period shorter than (upper panels) 2 hours and (lower panels) 20 minutes. The UT time is 3 hour on January 30th.

Appendix A Species dependent thermodynamics

Lauritzen et al. (2018) derived energy consistent equations of motion and equation of state for moist air including water vapor and condensates. Here we expand that framework for species dependent dry air. The implementation is such that the user can specify a list of major species via the namelist. Let $\mathcal{L}_{dry}$ be the set of species that make up dry air that in this study is given by

$$\mathcal{L}_{dry} = \{O, O_2, H, N_2\}\,. \tag{A1}$$

The framework can easily be extended to include more species in dry air. The set of all components of moist air is given by

$$\mathcal{L}_{all} = \mathcal{L}_{dry} \cup \mathcal{L}_{H_2O}, \tag{A2}$$

where $\mathcal{L}_{H_2O}$ is the set of water species (water vapor, cloud liquid, ice, rain, and snow):

$$\mathcal{L}_{H_2O} = \{'wv','cl','ci','rn','sn'\}\,. \tag{A3}$$

The dry mixing ratio for each species is defined as

$$m^{(\ell)} \equiv \frac{\rho^{(\ell)}}{\rho^{(d)}}, \tag{A4}$$

where $\rho^{(d)}$ is the mass of dry air per unit volume of moist air and $\rho^{(\ell)}$ is the mass of the species ℓ per unit volume of moist air. Note that the mixing ratio for dry air is one by definition

$$\sum_{\ell \in \mathcal{L}_{dry}} m^{(\ell)} = 1, \tag{A5}$$

and that the mixing ratio for N_2 is derived from the other components of dry air

$$m^{(N_2)} = 1 - m^{(O)} - m^{(O_2)} - m^{(H)}. \tag{A6}$$

The specific (moist) mixing ratios are given by

$$q^{(\ell)} \equiv \frac{\rho^{(\ell)}}{\rho}, \tag{A7}$$

where ρ is the density of moist air.

A1 Species dependent specific heat for dry air

The specific heat at constant pressure for species ℓ is given by

$$c_p^{(\ell)} = \frac{1}{2} R_d \frac{dof^{(\ell)}}{\mathcal{M}^{(\ell)}}, \tag{A8}$$

where R_d is the universal gas constant, $\mathcal{M}^{(\ell)}$ is the molecular mass of species ℓ and $dof^{(\ell)}$ is degrees of freedom:

$$dof = \{5, 7, 7, 5\} \text{ for set } \mathcal{L}_{dry}. \tag{A9}$$

The formula for the specific heat of dry air at constant pressure is simply the sum of the specific heats for each major species

$$c_p^{(d)} = \textstyle\sum_{\ell \in \mathcal{L}_{dry}} c_p^{(\ell)} m^{(\ell)}. \tag{A10}$$

The generalized specific heat for species dependent moist air is then

$$c_p = \frac{c_p^{(d)} + \sum_{\ell \in \mathcal{L}_{H_2O}} c_p^{(\ell)} m^{(\ell)}}{\sum_{\ell \in \mathcal{L}_{all}} m^{(\ell)}}, \tag{A11}$$

$$= \sum_{\ell \in \mathcal{L}_{all}} c_p^{(\ell)} q^{(\ell)}, \tag{A12}$$

(Lauritzen et al., 2018). There is currently a discrepancy between CAM physics (that assumes that $\mathcal{L}_{H_2O} = \{'wv'\}$) and the spectral-element dynamical core that includes all forms of water in the thermodynamics.

A2 Species dependent R for dry air

The definition of the gas constant for dry air, according to the original definition from kinetic theory, is

$$R^{(d)} = R_d \sum_{\ell \in \mathcal{L}_{dry}} \left[\frac{m^{(\ell)}}{\mathcal{M}^{(\ell)}} \right], \tag{A13}$$

$$= \sum_{\ell \in \mathcal{L}_{dry}} \frac{R_d}{\mathcal{M}^{(\ell)}} m^{(\ell)}, \tag{A14}$$

$$= \sum_{\ell \in \mathcal{L}_{dry}} R^{(\ell)} m^{(\ell)} \tag{A15}$$

where $R^{(\ell)}$ is given by

$$R^{(\ell)} = \frac{R_d}{\mathcal{M}^{(\ell)}}, \text{ for } \ell \in \mathcal{L}_{dry}, \tag{A16}$$

in which case the generalized R becomes

$$R = \frac{R^{(d)} + \sum_{\ell \in \mathcal{L}_{H_2O}} R^{(\ell)} m^{(\ell)}}{\sum_{\ell \in \mathcal{L}_{all}} m^{(\ell)}}, \tag{A17}$$

$$= \sum_{\ell \in \mathcal{L}_{all}} \left[R^{(\ell)} q^{(\ell)} \right], \tag{A18}$$

where $R^{(\ell)} = 0$ for non-gas components of air (condensates).

A3 Virtual temperature

Let $\mathcal{L}_{gas}$ be the set of gaseous components of dry air. Each gaseous component of air satisfies in the ideal gas law

$$p^{(\ell)} V^{(gas)} = V \rho^{(\ell)} R^{(\ell)} T, \text{for } \ell \in \mathcal{L}_{gas} \tag{A19}$$

where $p^{(\ell)}$ is the partial pressure of gas ℓ, V is the volume of moist air and $V^{(gas)}$ the volume of the gaseous components of moist air. Applying Dalton's law of partial pressures, the total pressure is given by

$$\begin{aligned}
p &= \sum_{\ell \in \mathcal{L}_{gas}} p^{(\ell)}, \\
&= \frac{V}{V^{(gas)}} \sum_{\ell \in \mathcal{L}_{gas}} \left[\rho^{(\ell)} R^{(\ell)} T \right], \text{ using (A19)} \\
&= \frac{V}{V^{(gas)}} \rho^{(d)} R^{(d)} T \sum_{\ell \in \mathcal{L}_{gas}} \left[\frac{\rho^{(\ell)}}{\rho^{(d)}} \frac{R^{(\ell)}}{R^{(d)}} \right], \text{ `pull' out } \rho^{(d)} R^{(d)}, \\
&\approx \rho^{(d)} R^{(d)} T \sum_{\ell \in \mathcal{L}_{gas}} \left[\frac{\rho^{(\ell)}}{\rho^{(d)}} \frac{R^{(\ell)}}{R^{(d)}} \right], \text{ assume condensates occupy 0 volume } \frac{V}{V^{(gas)}} = 1, \\
&= \rho^{(d)} R^{(d)} T \sum_{\ell \in \mathcal{L}_{gas}} \left[m^{(\ell)} \frac{R^{(\ell)}}{R^{(d)}} \right], \text{ use } m^{(\ell)} \equiv \frac{\rho^{(\ell)}}{\rho^{(d)}}, \\
&= \rho R^{(d)} T \sum_{\ell \in \mathcal{L}_{gas}} \left[\frac{m^{(\ell)} \frac{R^{(\ell)}}{R^{(d)}}}{\sum_{\mathcal{L}_{all}} m^{(\ell)}} \right], \text{ using } \rho = \rho^{(d)} \sum_{\mathcal{L}_{all}} m^{(\ell)}, \\
&= \rho R^{(d)} T \sum_{\ell \in \mathcal{L}_{all}} \left[\frac{m^{(\ell)} \frac{R^{(\ell)}}{R^{(d)}}}{\sum_{\mathcal{L}_{all}} m^{(\ell)}} \right], \text{ since } R^{(\ell)} = 0 \text{ for non-gas components}, \\
&= \rho R^{(d)} T \frac{R}{R^{(d)}}, \text{ where } R^{(d)} \text{ is given by (A17)}, \\
&= \rho R^{(d)} T_v,
\end{aligned}$$

where the virtual temperature is given by

$$\begin{aligned} T_v &= T\frac{R}{R^{(d)}}, && \text{(A20)}\\ &= T\left[\frac{1+\left(\frac{R^{(wv)}}{R^{(d)}}\right)m^{(wv)}}{\sum_{\ell\in\mathcal{L}_{all}} m^{(\ell)}}\right], && \text{(A21)}\end{aligned}$$

and $R^{(d)}$ is given in (A17). We can rewrite (A21) as

$$\begin{aligned} T_v &= T\left[\frac{1+\left(\frac{R^{(wv)}}{R^{(d)}}\right)m^{(wv)}}{\sum_{\ell\in\mathcal{L}_{all}} m^{(\ell)}}\right] && \text{(A22)}\\ &= T\left[\frac{1+m^{(wv)}+\left(\frac{R^{(wv)}}{R^{(d)}}\right)m^{(wv)}-m^{(wv)}}{\sum_{\ell\in\mathcal{L}_{all}} m^{(\ell)}}\right] && \text{(A23)}\\ &= T\left[\frac{1+m^{(wv)}+\left\{\left(\frac{R^{(wv)}}{R^{(d)}}\right)-1\right\}m^{(wv)}}{\sum_{\ell\in\mathcal{L}_{all}} m^{(\ell)}}\right] && \text{(A24)}\\ &= T\left[\frac{1+m^{(wv)}}{\sum_{\ell\in\mathcal{L}_{all}} m^{(\ell)}}+\frac{\left\{\left(\frac{R^{(wv)}}{R^{(d)}}\right)-1\right\}m^{(wv)}}{\sum_{\ell\in\mathcal{L}_{all}} m^{(\ell)}}\right] && \text{(A25)}\\ &= T\left[\frac{1+m^{(wv)}}{\sum_{\ell\in\mathcal{L}_{all}} m^{(\ell)}}+\left\{\left(\frac{R^{(wv)}}{R^{(d)}}\right)-1\right\}q^{(wv)}\right] && \text{(A26)}\end{aligned}$$

So if and only if water vapor is the only non-dry component of dry air, i.e.

$$\sum_{\ell\in\mathcal{L}_{all}} m^{(\ell)} = 1+m^{(wv)}, \tag{A27}$$

then (A21) can be written as

$$T_v = T\left[1+\left(\frac{R^{(wv)}}{R^{(d)}}-1\right)q^{(wv)}\right], \tag{A28}$$

which is the formula used in CAM physics but not the spectral-element dynamical core.

Appendix B Molecular viscosity and thermal conductivity

The implementation of molecular viscosity and thermal conductivity in WACCM-X is split into a horizontal part (handled by the dynamical core) and vertical (performed in physics). That is, for the molecular viscosity the dynamical core solves

$$\frac{d\vec{v}}{dt} = \frac{1}{\rho}\nabla_z\cdot\left(kmvis\nabla_z\vec{v}\right), \tag{B1}$$

where $kmvis$ is a dynamic viscosity coefficient which is a function of the major species, and physics solves

$$\frac{d\vec{v}}{dt} = \frac{1}{\rho}\frac{d}{dz}\left(kmvis\frac{d\vec{v}}{dz}\right). \tag{B2}$$

Since WACCM-X uses pressure coordinates we use the chain rule to rewrite the horizontal gradient term

$$\nabla_p\vec{v} = \nabla_z\vec{v}+\left(\frac{\partial p}{\partial z}\right)(\nabla_p z)\left(\frac{\partial\vec{v}}{\partial p}\right), \tag{B3}$$

and use the hydrostatic relation

$$\frac{\partial p}{\partial z} = -\rho g, \tag{B4}$$

(where g is gravity) to rewrite the horizontal molecular viscosity equation

$$\nabla_z \vec{v} = \nabla_p \vec{v} + \rho \nabla_p \Phi \left(\frac{\partial \vec{v}}{\partial p} \right), \tag{B5}$$

where $\Phi = gz$ is the geopotential. The second term on the right-hand side of (B5) is found to be much smaller than the first throughout the computational domain, and has been neglected in the current implementation. Hence the operators are applied along pressure surfaces rather than z surfaces. For the vertical a transformation to pressure coordinates yields

$$\frac{d\vec{v}}{dt} \quad = \quad g^2 \frac{d}{dp} \left(kmvis\, \rho \frac{d\vec{v}}{dp} \right). \tag{B6}$$

A unified infrastructure has been implemented so that the dynamical core (”horizontal”) and physics package (vertical) fetch the viscosity coefficient (*kmvis*) coefficients from the same code module.

The frictional dissipation of kinetic energy is ultimately turned into heating at the molecular scale. In WACCM-X the change in kinetic energy due to molecular viscosity is turned into heat at each grid point

$$\Delta T_{heat} = -\frac{1}{c_p} \left(K^{(new)} - K^{(old)} \right) \tag{B7}$$

where $K^{(old)} = \frac{1}{2}\vec{v}^2$ is specific kinetic energy before applying the molecular viscosity operator to $\vec{v}$ and $K^{(new)}$ is after. While this guarantees a closed energy budget it is not entirely correct since the kinetic energy equation terms associated with molecular viscosity have a dissipative and a diffusive term; only the dissipative term should be added as heating (Bister & Emanuel, 1998). A way to do this rigorously and consistently in spherical geometry is presented in Becker and Burkhardt (2007).

The thermal conductivity equations take the same form as molecular viscosity except for a c_p term in equations

$$\frac{d}{dt}(c_p T) = \frac{1}{\rho} \nabla_z (kmcnd \nabla_z T), \tag{B8}$$

and

$$\frac{d}{dt}(c_p T) = \frac{1}{\rho} \frac{d}{dz} \left(kmcnd \frac{dT}{dz} \right). \tag{B9}$$

where *kmcnd* is the conductivity coefficient that is a function of the major species. The transformation to pressure coordinates is the same as outlined above and not repeated here.

Appendix C Vertical profiles for artificial viscosity (sponge layer damping)

It was found challenging to stabilize WACCM-X likely due to the less diffusive characteristics of the spectral-element dynamical core (compared to the finite-volume dynamical core) and perhaps excessively large tendencies from the parameterizations (the latter was not investigated in detail).

The spectral-element dynamical core by default uses constant hypverviscosity ($\nabla^4_{\psi^{(ref)}}$) applied to all prognostic variables $\psi = T$ (temperature),$\psi = \Delta p$ (pressure-level thickness), divergence $\psi = \delta$ and vorticity $\psi = \zeta$. For a nominal 1° resolution the constant reference values for fourth-order hyperviscosity are

$$\begin{aligned} \nu_\delta^{(ref)} &= 2.5 \times 10^{15}\, m^4/s, \\ \nu_\zeta^{(ref)} &= 0.5 \times 10^{15}\, m^4/s, \\ \nu_T^{(ref)} = \nu_{\Delta p}^{(ref)} \equiv \nu_{\Delta x = 1^\circ}^{(ref)} &= 1.0 \times 10^{15}\, m^4/s, \end{aligned} \tag{C1}$$

(reference hyperviscosity coefficients for nominally 1° resolution; $\Delta x^{(ref)} \equiv 110km$) and are scaled for other resolutions using

$$\begin{aligned}\nu_\delta^{(ref)} &= 2.5 \times \Upsilon, \\ \nu_\zeta^{(ref)} &= 0.5 \times \Upsilon, \\ \nu_T^{(ref)} = \nu_{\Delta p}^{(ref)} &= 1.0 \times \Upsilon,\end{aligned} \tag{C2}$$

(reference hyperviscosity coefficients for any resolution)

where

$$\Upsilon \equiv \nu^{(scaling)} \left[\left(\frac{30}{ne} \right) \nu_{\Delta x = 1^\circ}^{(ref)} \right]^\lambda \tag{C3}$$

and

$$\nu^{(scaling)} = \left[\frac{R}{R^{(Earth)}} \right] \nu_{\Delta x = 1^\circ}^{(ref)} \left[\Delta x^{(ref)} \right]^{-\lambda} \tag{C4}$$

where $\lambda \equiv \frac{1}{\log_{10} 2}$ is the scaling coefficient (which ensures that viscosity coefficients decrease a logarithmic decade for a doubling of resolution), $\nu_{\Delta x=1^\circ}^{(ref)}$ is a reference value for viscosity at 1° resolution given in (C2) and associated average grid spacing $\Delta x^{(ref)} = 110km$. Since spectral-elements is also run on other planets the viscosity coefficients need to be scaled accordingly. Hence we have introduced R, which is the mean radius of the planet in question, and $R^{(Earth)}$ is the mean radius of Earth. The resolution is specified in terms of number of elements along a cubed-sphere side, ne. For 1° $ne = 30$ and for 0.25° $ne = 120$ and the resulting viscosity coefficients are $\nu_\delta^{(ref)} = 2.5 \times 10^{13}$, $\nu_\zeta^{(ref)} = 0.5 \times 10^{13}$ and $\nu_T^{(ref)} = \nu_{\Delta p}^{(ref)} = 1.0 \times 10^{13}$. Some of these values are adjusted for WACCM-X:

$$\begin{aligned}\nu_\delta^{(ref)} &= 1.5 \times 10^{13}\, m^4/s, \\ \nu_\zeta^{(ref)} &= 1.0 \times 10^{13}\, m^4/s, \\ \nu_T^{(ref)} = \nu_{\Delta p}^{(ref)} &= 1.0 \times 10^{13}\, m^4/s,\end{aligned}$$

these values were chosen empirically to maintain numerical stability.

In addition there is increased Laplacian damping (∇^2) near the model top using the following coefficient

$$\mu_\psi(k) = \Gamma^{(\mu)}(k)\mu^{(ref)}, \text{ where } \psi = T, \vec{v}, \Delta p, \tag{C5}$$

if $\Gamma^{(\mu)}(k) > 0.15$ else $\mu^{(\mu)}(k) = 0$. The reference value $\mu^{(ref)}$ is specified via the namelist variable `se_nu_top` (for WACCM-X $\mu^{(ref)} = 1E6m^2/s$ and for any other configuration it is $\mu^{(ref)} = 1.25E5m^2/s$). The scaling function $\Gamma^{(\mu)}$ is given by

$$\Gamma^{(\mu)}(k) = 8 \left\{ 1 + \tanh \left[\log \left(\frac{p_{top}}{p_k} \right) \right] \right\}, \tag{C6}$$

(Lauritzen et al., 2011) where p_{top} is the pressure at the model top and p_k is the mid pressure in level k.

Unfortunately this level of damping was found insufficient for stabilizing WACCM-X. Even drastic increases in $\mu^{(ref)}$ were found unsuccessful in terms of stability. By trial and error stability was achieved by increasing ∇^4 damping in the top model layers using the following scaling function

$$\Gamma^{(\nu)}(k) = \frac{1}{2} \left\{ 1 + \tanh \left[2 \log \left(\frac{p_{k_s}}{p_k} \right) \right] \right\} \tag{C7}$$

where k_s is the mid-point of the sponge given by namelist variable

$$k_s = \texttt{se\_sponge\_del4\_lev}. \tag{C8}$$

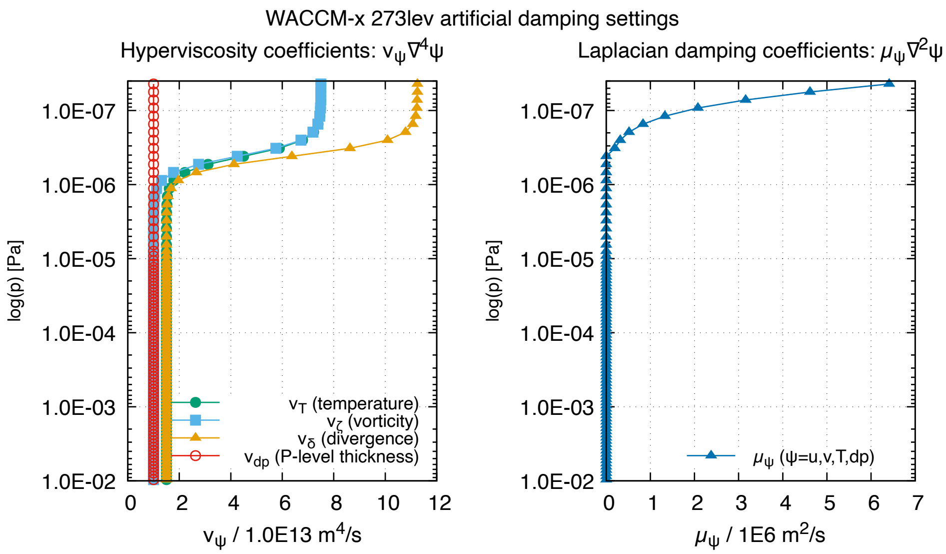

Figure C1: Left plot shows the hyperviscosity coefficient (ν_ψ, $\psi = \delta, \zeta, T, \Delta p$) in units of $1 \times 10^{13} m^4/s$ as a function of pressure (Pa). The right Figure is the Laplacian sponge layer diffusion coefficient (μ_ψ, $\psi = \vec{v}, T, \Delta p$) in units of $1E6 m^2/s$ as a function of pressure. The artificial Laplacian damping coefficient is much smaller than the physical molecular viscosity and thermal conductivity coefficients.

For WACCM-X we use $k_s = 10$ (for model tops up to 140km we use $k_s = 3$). The following damping coefficients, ν_ψ, are used for ∇^4 operator on divergence (δ), vorticity (ζ) and temperature (T)

$$\nu_\psi(k) = \left[1 - \Gamma^{(\nu)}(k)\right] \nu_\psi^{(ref)} + \Gamma^{(\nu)}(k) \nu_\psi^{(max)}, \quad \text{where } \psi = \delta, \zeta, \mathrm{T} \tag{C9}$$

where the maximum damping coefficients (for model tops above ∼42km, i.e. WACCM and WACCM-X)[1] are

$$\nu_\delta^{(max)} = 7.5 \nu_{\Delta p}^{(ref)}, \text{ namelist } \texttt{se\_sponge\_del4\_nu\_div\_fac=7.5}, \tag{C10}$$
$$\nu_\zeta^{(max)} = 5.0 \nu_{\Delta p}^{(ref)}, \text{ namelist } \texttt{se\_sponge\_del4\_nu\_fac=5.0}, \tag{C11}$$
$$\nu_T^{(max)} = 5.0 \nu_{\Delta p}^{(ref)}, \text{ namelist } \texttt{se\_sponge\_del4\_nu\_fac=5.0}, \tag{C12}$$

The damping coefficients as a function of pressure are shown in Figure C1

Acknowledgments

This work is partially funded by the NCAR System for Integrated Modeling of the Atmosphere (SIMA) project. HLL acknowledges partial support by NASA Grants 80NSSC20K1323, 80NSSC20K0601, 80NSSC20K0633, and 80NSSC21K1305. National Center for Atmospheric Research is a major facility sponsored by the National Science Foundation under Cooperative Agreement No. 1852977. Numerical simulations were performed on NWSC/NCAR Cheyenne Supercomputers with computing resources provided by the NCAR Strategic Capability (NSC) allocation and the Computational and Information Systems Laboratory (CISL) at NCAR. NCAR CESM/WACCM is an open-source community model, and

[1] for model configurations with model tops below ∼42 km `se_sponge_del4_nu_div_fac=4.5` and `se_sponge_del4_nu_div_fac=1.0`

is available at `https://doi.org/10.5065/D67H1H0V`. Model output used for this study is available through GLOBUS (shared end point: `https://tinyurl.com/3hnwjz93`).

References

Akmaev, R. A. (2011). Whole atmosphere modeling: Connecting terrestrial and space weather. *Rev. Geophys.*, *49*. doi: 10.1029/2011RG000364

Azeem, I., Walterscheid, R. L., & Crowley, G. (2018). Investigation of acoustic waves in the ionosphere generated by a deep convection system using distributed networks of gps receivers and numerical modeling. *Geophysical Research Letters*, *45*, 8014-8021. doi: 10.1029/2018GL078107

Azeem, I., Yue, J., Hoffmann, L., Miller, S. D., Straka, W. C., & Crowley, G. (2015). Multisensor profiling of a concentric gravity wave event propagating from the troposphere to the ionosphere. *Geophysical Research Letters*, *42*, 7874–7880. (2015GL065903) doi: 10.1002/2015GL065903

Becker, E., & Burkhardt, U. (2007). Nonlinear horizontal diffusion for GCMs. *Monthly Weather Review*, *135*(4), 1439 - 1454. Retrieved from `https://journals.ametsoc.org/view/journals/mwre/135/4/mwr3348.1.xml` doi: 10.1175/MWR3348.1

Becker, E., & Vadas, S. E. (2018). Secondary gravity waves in the winter mesosphere: Results from a high-resolution global circulation model. *Journal of Geophysical Research: Atmospheres*, *123*, 2605?2627. doi: 10.1002/2017JD027460

Becker, E., & Vadas, S. L. (2020). Explicit global simulation of gravity waves in the thermosphere. *Journal of Geophysical Research: Space Physics*, *125*, e2020JA028034. doi: https://doi.org/10.1029/2020JA028034

Becker, E., Vadas, S. L., Bossert, K., Harvey, V. L., Zülicke, C., & Hoffmann, L. (2022). A high-resolution whole-atmosphere model with resolved gravity waves and specified large-scale dynamics in the troposphere and stratosphere. *Journal of Geophysical Research: Atmospheres*, *127*(2), e2021JD035018.

Bister, M., & Emanuel, K. A. (1998). Dissipative heating and hurricane intensity. *Meteorology and Atmospheric Physics*, *65*, 233?240. doi: https://doi.org/10.1007/BF01030791

Borchert, S., Zhou, G., Baldauf, M., Schmidt, H., Zängl, G., & Reinert, D. (2019). The upper-atmosphere extension of the icon general circulation model (version: ua-icon-1.0). *Geoscientific Model Development*, *12*(8), 3541–3569.

Catling, D. C., & Kasting, J. F. (2017). *Atmospheric evolution on inhabited and lifeless worlds*. Cambridge University Press.

Codrescu, M., Fuller-Rowell, T., & Foster, J. (1995). On the importance of e-field variability for joule heating in the high-latitude thermosphere. *Geophysical Research Letters*, *22*(17), 2393–2396.

Emmert, J. T., Picone, J. M., Lean, J. L., & Knowles, S. H. (2004). Global change in the thermosphere: Compelling evidence of a secular decrease in density. *Journal of Geophysical Research: Space Physics*, *109*. doi: 10.1029/2003JA010176

Emmert, J. T., Picone, J. M., & Meier, R. R. (2008). Thermospheric global average density trends, 1967?2007, derived from orbits of 5000 near-earth objects. *Geophysical Research Letters*, *35*. doi: 10.1029/2007GL032809

Ern, M., Preusse, P., Gille, J. C., Hepplewhite, C. L., Mlynczak, M. G., III, J. M. R., & Riese, M. (2011). Implications for atmospheric dynamics derived from global observations of gravity wave momentum flux in stratosphere and mesosphere. *Journal of Geophysical Research*, *116*. doi: 10.1029/2011JD015821

Ern, M., Trinh, Q. T., Preusse, P., Gille, J. C., Mlynczak, M. G., Russell III, J. M., & Riese, M. (2018). Gracile: a comprehensive climatology of atmospheric gravity wave parameters based on satellite limb soundings. *Earth System Science Data*, *10*, 857–892. doi: 10.5194/essd-10-857-2018

Forbes, J. M., Bruinsma, S. L., Doornbos, E., & Zhang, X. (2016). Gravity wave-induced variability of the middle thermosphere. *Journal of Geophysical Research: Space Physics*, *121*, 6914-6923. doi: 10.1002/2016JA022923

Gasperini, F., Hagan, M. E., & Zhao, Y. (2017). Evidence of tropospheric 90day oscillations in the thermosphere. *Geophysical Research Letters*, *44*, 10,125-10,133. doi: 10.1002/2017GL075445

Gasperini, F., Liu, H., & McInerney, J. (2020). Preliminary evidence of madden-julian oscillation effects on ultrafast tropical waves in the thermosphere. *Journal of Geophysical Research: Space Physics*, *125*, e2019JA027649. doi: 10.1029/2019JA027649

Geller, M. A., Alexander, M. J., Love, P. T., Bacmeister, J., Ern, M., Hertzog, A., … Zhou, T. (2013). A comparison between gravity wave momentum fluxes in observations and climate models. *Journal of Climate*, *26*, 6383-6405. doi: 10.1175/JCLI-D-12-00545.1

Gettelman, A., Mills, M. J., Kinnison, D. E., Garcia, R. R., Smith, A. K., Marsh, D. R., … Randel, W. J. (2019). The whole atmosphere community climate model version 6 (waccm6). *Journal of Geophysical Research: Atmospheres*, *124*, 12380-12403. doi: https://doi.org/10.1029/2019JD030943

Herrington, A. R., Lauritzen, P. H., Reed, K. A., Goldhaber, S., & Eaton, B. E. (2019). Exploring a lower-resolution physics grid in cam-se-cslam. *Journal of Advances in Modeling Earth Systems*, *11*(7), 1894–1916.

Herrington, A. R., Lauritzen, P. H., Taylor, M. A., Goldhaber, S., Eaton, B. E., Bacmeister, J. T., … Ullrich, P. A. (2019). Physics–dynamics coupling with element-based high-order galerkin methods: Quasi-equal-area physics grid. *Monthly Weather Review*, *147*(1), 69–84.

Huang, C. S., & Kelley, M. C. (1996a). Nonlinear evolution of equatorial spread-f. 1. on the role of plasma instabilities and spatial resonance associated with gravity wave seeding. *Journal of Geophysical Research*, *101*, 283-292.

Huang, C. S., & Kelley, M. C. (1996b). Nonlinear evolution of equatorial spread-f. 2. gravity wave seeding of rayleigh-taylor instability. *Journal of Geophysical Research*, *101*, 293-302.

Huba, J. D., & Liu, H.-L. (2020). Global modeling of equatorial spread f with sami3/waccm-x. *Geophysical Research Letters*, *47*, e2020GL088258. doi: 10.1029/2020GL088258

Hysell, D. L., Kelley, M. C., Swartz, W. E., & Woodman, R. F. (1990). Seeding and layering of equatorial spread f by gravity waves. *Journal of Geophysical Research: Space Physics*, *95*, 17253-17260. doi: 10.1029/JA095iA10p17253

Jin, H., Miyoshi, Y., Fujiwara, H., Shinagawa, H., Terada, K., Terada, N., … Saito, A. (2011). Vertical connection from the tropospheric activities to the ionospheric longitudinal structure simulated by a new earth's whole atmosphere-ionosphere coupled model. *Journal of Geophysical Research: Space Physics*, *116*. doi: 10.1029/2010JA015925

John, S. R., & Kumar, K. K. (2012). Timed/saber observations of global gravity wave climatology and their interannual variability from stratosphere to mesosphere lower thermosphere. *Climate dynamics*, *39*(6), 1489–1505.

Jones Jr., M., Siskind, D. E., Drob, D. P., McCormack, J. P., Emmert, J. T., Dhadly, M. S., … Jacobi, C. (2020). Coupling from the middle atmosphere to the exobase: Dynamical disturbance effects on light chemical species. *Journal of Geophysical Research: Space Physics*, *125*, e2020JA028331. doi: 10.1029/2020JA028331

Kelley, M. C., Larsen, M. F., LaHoz, C., & McClure, J. P. (1981). Gravity wave initiation of equatorial spread f: A case study. *Journal of Geophysical Research: Space Physics*, *86*, 9087-9100. doi: 10.1029/JA086iA11p09087

Krall, J., Huba, J. D., & Fritts, D. C. (2013). On the seeding of equatorial spread f by gravity waves. *Geophysical Research Letters*, *40*, 661–664. doi: 10.1002/grl.50144

Lauritzen, P. H., Mirin, A., Truesdale, J., Raeder, K., Anderson, J., Bacmeister, J., & Neale, R. B. (2011). Implementation of new diffusion/filtering operators in the CAM-FV dynamical core. *The International Journal of High Performance Computing Applications*. doi: 10.1177/1094342011410088

Lauritzen, P. H., Nair, R. D., Herrington, A. R., Callaghan, P., Goldhaber, S., Dennis, J. M., ... Tribbia, J. J. (2018). Ncar release of cam-se in cesm2.0: A reformulation of the spectral element dynamical core in dry-mass vertical coordinates with comprehensive treatment of condensates and energy. *Journal of Advances in Modeling Earth Systems*, *10*, 1537-1570. doi: https://doi.org/10.1029/2017MS001257

Lauritzen, P. H., Taylor, M. A., Overfelt, J., Ullrich, P. A., Nair, R. D., Goldhaber, S., & Kelly, R. (2017). Cam-se–cslam: Consistent coupling of a conservative semi-lagrangian finite-volume method with spectral element dynamics. *Monthly Weather Review*, *145*(3), 833–855.

Liu, H., Pedatella, N., & Hocke, K. (2017). Medium-scale gravity wave activity in the bottomside f region in tropical regions. *Geophysical Research Letters*, *44*, 7099-7105. doi: 10.1002/2017GL073855

Liu, H.-L. (2007). On the large wind shear and fast meridional transport above the mesopause. *Geophysical Research Letters*, *34*. (L08815) doi: 10.1029/2006GL028789

Liu, H.-L. (2016). Variability and predictability of the space environment as related to lower atmosphere forcing. *Space Weather*, *14*, 634–658. (2016SW001450) doi: 10.1002/2016SW001450

Liu, H.-L. (2019). Quantifying gravity wave forcing using scale invariance. *Nature Communications*, *10*, 2605. doi: 10.1038/s41467-019-10527-z

Liu, H.-L. (2021). Effective vertical diffusion by atmospheric gravity waves. *Geophysical Research Letters*, *48*(1), e2020GL091474.

Liu, H.-L., Bardeen, C. G., Foster, B. T., Lauritzen, P., Liu, J., Lu, G., ... Wang, W. (2018). Development and validation of the whole atmosphere community climate model with thermosphere and ionosphere extension (waccm-x 2.0). *Journal of Advances in Modeling Earth Systems*, *10*, 381-402. doi: 10.1002/2017MS001232

Liu, H.-L., McInerney, J. M., Santos, S., Lauritzen, P. H., Taylor, M. A., & Pedatella, N. M. (2014). Gravity waves simulated by high-resolution Whole Atmosphere Community Climate Model. *Geophysical Research Letters*, *41*, 9106–9112. (2014GL062468) doi: 10.1002/2014GL062468

Liu, H.-L., & Roble, R. G. (2002). A study of a self-generated stratospheric sudden warming and its mesospheric/lower thermospheric impacts using coupled TIME-GCM/CCM3. *Journal of Geophysical Research*, *107*. doi: 10.1029/2001JD001533

McClure, J. P., Singh, S., Bamgboye, D. K., Johnson, F. S., & Kil, H. (1998). Occurrence of equatorial f region irregularities: Evidence for tropospheric seeding. *Journal of Geophysical Research: Space Physics*, *103*, 29119-29135. doi: 10.1029/98JA02749

Meier, R. (2021). The thermospheric column o/n2 ratio. *Journal of Geophysical Research: Space Physics*, *126*(3), e2020JA029059.

Miyoshi, Y., Jin, H., Fujiwara, H., & Shinagawa, H. (2018). Numerical study of traveling ionospheric disturbances generated by an upward propagating gravity wave. *Journal of Geophysical Research: Space Physics*, *123*, 2141-2155. doi: 10.1002/2017JA025110

Nishioka, M., Tsugawa, T., Kubota, M., & Ishii, M. (2013). Concentric waves and short-period oscillations observed in the ionosphere after the 2013

Moore EF5 tornado. *Geophysical Research Letters*, *40*, 5581–5586. doi: 10.1002/2013GL057963

Okui, H., Sato, K., & Watanabe, S. (2022). Contribution of gravity waves to universal vertical wavenumber ($\sim m^{-3}$) spectra revealed by a gravity-wave-permitting general circulation model. *Journal of Geophysical Research: Atmospheres*, e2021JD036222.

Park, J., Lühr, H., Lee, C., Kim, Y. H., Jee, G., & Kim, J.-H. (2014). A climatology of medium-scale gravity wave activity in the midlatitude/low-latitude daytime upper thermosphere as observed by champ. *Journal of Geophysical Research: Space Physics*, *119*, 2187-2196. doi: 10.1002/2013JA019705

Pedatella, N. M., Anderson, J. L., Chen, C. H., Raeder, K., Liu, J., Liu, H.-L., & Lin, C. H. (2020). Assimilation of ionosphere observations in the whole atmosphere community climate model with thermosphere-ionosphere extension (waccmx). *Journal of Geophysical Research: Space Physics*, *125*, e2020JA028251. doi: https://doi.org/10.1029/2020JA028251

Pedatella, N. M., Fuller-Rowell, T., Wang, H., Jin, H., Miyoshi, Y., Fujiwara, H., … Goncharenko, L. (2014). The neutral dynamics during the 2009 sudden stratosphere warming simulated by different whole atmosphere models. *Journal of Geophysical Research: Space Physics*, *119*, 1306-1324. doi: 10.1002/2013JA019421

Pedatella, N. M., & Liu, H.-L. (2018). The influence of internal atmospheric variability on the ionosphere response to a geomagnetic storm. *Geophysical Research Letters*, *45*(10), 4578–4585.

Pedatella, N. M., Raeder, K., Anderson, J. L., & Liu, H.-L. (2014). Ensemble data assimilation in the whole atmosphere community climate model. *Journal of Geophysical Research*, *119*, 9793-9809. doi: 10.1002/2014JD021776

Pitteway, M. L. V., & Hines, C. O. (1963). The viscous damping of atmospheric gravity waves. *Canadian Journal of Physics*, *41*, 1935-1948. doi: 10.1139/p63-194

Qian, L. Y., Solomon, S. C., & Kane, T. J. (2009). Seasonal variation of thermospheric density and composition. *Journal of Geophysical Research*, *114*. doi: 10.1029/2008JA013643

Randall, C. E., Harvey, V. L., Singleton, C. S., Bernath, P. F., Boone, C. D., & Kozyra, J. U. (2006). Enhanced nox in 2006 linked to strong upper stratospheric arctic vortex. *Geophysical Research Letters*, *33*. doi: 10.1029/2006GL027160

Randall, C. E., Harvey, V. L., Siskind, D. E., France, J., Bernath, P. F., Boone, C. D., & Walker, K. A. (2009). NO_x descent in the Arctic middle atmosphere in early 2009. *Geophysical Research Letters*, *36*. doi: 10.1029/2009GL039706

Retterer, J. M., & Roddy, P. (2014). Faith in a seed: on the origins of equatorial plasma bubbles. *Annales Geophysicae*, *32*, 485–498. doi: 10.5194/angeo-32-485-2014

Richmond, A. D. (1995). Ionospheric electrodynamics using magnetic apex coordinates. *J. Geomagn. Geoelectr.*, *47*, 191–212.

Richter, J. H., Glanville, A. A., Edwards, J., Kauffman, B., Davis, N. A., Jaye, A., … Oleson, K. W. (2022). Subseasonal earth system prediction with cesm2. *Weather and Forecasting*, *37*, 797 - 815. doi: 10.1175/WAF-D-21-0163.1

Roble, R. G., & Dickinson, R. E. (1989). How will changes in carbon-dioxide and methane modify the mean structure of the mesosphere and thermosphere. *Geophysical Research Letters*, *16*, 1441-1444.

Savitzky, A., & Golay, M. J. (1964). Smoothing and differentiation of data by simplified least squares procedures. *Analytical chemistry*, *36*(8), 1627–1639.

Solomon, S. C., Liu, H.-L., Marsh, D. R., McInerney, J. M., Qian, L., & Vitt, F. M. (2018). Whole atmosphere simulation of anthropogenic climate change. *Geophysical Research Letters*, *45*, 1567-1576. doi: 10.1002/2017GL076950

Stober, G., Kuchar, A., Pokhotelov, D., Liu, H., Liu, H.-L., Schmidt, H., ... others (2021). Interhemispheric differences of mesosphere–lower thermosphere winds and tides investigated from three whole-atmosphere models and meteor radar observations. *Atmospheric chemistry and physics*, *21*(18), 13855–13902.

Strickland, D., Evans, J., & Paxton, L. (1995). Satellite remote sensing of thermospheric o/n2 and solar euv: 1. theory. *Journal of Geophysical Research: Space Physics*, *100*(A7), 12217–12226.

Swinbank, R., & Ortland, D. A. (2003). Compilation of wind data for the Upper Atmosphere Research Satellite (UARS) Reference Atmosphere Project. *Journal of Geophysical Research*, *108*. doi: doi:10.1029/2002JD003135

Taylor, M. J., Forbes, J., Fritts, D. C., Eckermann, S. D., Snively, J. B., Liu, H., ... others (2017). The atmospheric waves experiment (awe): Quantifying the impact of gravity waves on the edge of space. In *Agu fall meeting abstracts* (Vol. 2017, pp. SA31B–01).

Theurich, G., DeLuca, C., Campbell, T., Liu, F., Saint, K., Vertenstein, M., ... Dunlap, R. (2016). The earth system prediction suite: Toward a coordinated u.s. modeling capability. *Bulletin of the American Meteorological Society*, *97*, 1229 - 1247. doi: 10.1175/BAMS-D-14-00164.1

Vadas, S. L. (2007). Horizontal and vertical propagation and dissipation of gravity waves in the thermosphere from lower atmospheric and thermospheric sources. *Journal of Geophysical Research*, *112*. doi: doi:10.1029/2006JA011845

Vadas, S. L., & Becker, E. (2019). Numerical modeling of the generation of tertiary gravity waves in the mesosphere and thermosphere during strong mountain wave events over the southern andes. *Journal of Geophysical Research: Space Physics*, *124*, 7687-7718. doi: 10.1029/2019JA026694

Vadas, S. L., & Fritts, D. C. (2001). Gravity wave radiation and mean responses to local body forces in the atmosphere. *Journal of the Atmospheric Sciences*, *58*, 2249-2279.

Vadas, S. L., & Liu, H.-L. (2013). Numerical modeling of the large-scale neutral and plasma responses to the body forces created by the dissipation of gravity waves from 6 h of deep convection in Brazil. *Journal of Geophysical Research*, *118*, 2593-2617. doi: 10.1002/jgra.50249

Verronen, P. T., Andersson, M. E., Marsh, D. R., Kovács, T., & Plane, J. M. C. (2016). Waccm-d?whole atmosphere community climate model with d-region ion chemistry. *Journal of Advances in Modeling Earth Systems*, *8*, 954-975. doi: 10.1002/2015MS000592

Wang, H., Fuller-Rowell, T. J., Akmaev, R. A., Hu, M., Kleist, D. T., & Iredell, M. D. (2011). First simulations with a whole atmosphere data assimilation and forecast system: The january 2009 major sudden stratospheric warming. *Journal of Geophysical Research: Space Physics*, *116*. doi: 10.1029/2011JA017081

Watanabe, S., & Miyahara, S. (2009). Quantification of the gravity wave forcing of the migrating diurnal tide in a gravity wave-resolving general circulation model. *Journal of Geophysical Research: Atmospheres*, *114*. (D07110) doi: 10.1029/2008JD011218

Wu, J., Feng, W., Liu, H.-L., Xue, X., Marsh, D. R., & Plane, J. M. C. (2021). Self-consistent global transport of metallic ions with waccm-x. *Atmospheric Chemistry and Physics*, *21*, 15619–15630. doi: 10.5194/acp-21-15619-2021